Climate Change Impacts on the Seasonal Variation of Hydro-Physical Characteristics in the Persian Gulf

Amir Reza Azarnivand[1] · Masoud Sadrinasab[1] · Mohsen Nasseri[2]

Abstract

Climate change affects atmospheric circulation patterns and intensifies recurrent extreme weather events across the globe. It has resulted in increasing air temperatures, rising sea levels, and alterations in precipitation patterns, which will immensely influence the hydro-environment regime in semi-enclosed water bodies (e.g., gulfs and estuaries). The Persian Gulf (PG), the world's hottest sea, is a regional hotspot for climate change. This study investigates how the interplay between climate change and the meteorological variables affects salinity, temperature, and density of water mass concerning water circulation patterns (WCPs) in PG. It contributes to representing a perspective of meteorological conditions over the region and projecting expected seasonal variations of PG hydro-physical properties at the beginning of the next decade. For these purposes, we used the downscaled data of 2030 under RCP2.6, RCP4.5, and RCP8.5 (representative concentration pathway) scenarios to run the hydrodynamic model and also used a 54-year time series (1948–2002) for reference model representing the historical state (HS). The findings project distinguishable temperature rise (reaching 37 °C in summer over vast areas), salinity rise in most parts (up to +5.4 practical salinity units relative to HS at the northwestern head in spring), and an increase in vertical density gradients leading to an increase in speeds of surface currents. These alterations in physical properties significantly influence chemical and biological processes in PG, potentially resulting in aquatic degradation and ecological issues. Therefore, the findings are remarkable for policymakers to develop adaptation management plans in the PG region in line with sustainable development goals.

Keywords Climate change · Water circulation · Statistical downscaling · Numerical modeling · Meteorological variables · Persian Gulf

Introduction

Global warming, as a consequence of natural and anthropogenic changes, has affected WCPs for decades, thereby highlighting the need for reassessments of previous projections of future climate and weather conditions. As one of the major stressors of ecosystems (Sala et al. 2000), climate change challenges our ability to devise sustainable management and conservation plans to maintain ecosystem services. It has begun to alter ocean conditions, particularly water temperature and various aspects of ocean biogeochemistry (Gattuso et al. 2015), which are coupled tightly with the physical processes (Hong and Shen 2012).

Gulfs are mainly affected by their surrounding landmass; therefore, the hydro-environment regime in such water bodies is closely linked with air temperature and precipitation patterns (Alosairi and Pokavanich 2017; Noori et al. 2019). Hence, alterations in meteorological variables such as air temperature, relative humidity, and precipitation play a crucial role in the future state of oceans and, particularly, gulfs.

The Persian Gulf (hereafter referred to as PG) in the Middle East, with 35% of the world's seaborne oil shipments (Al-Said et al. 2018) and over 50% of the global installed

✉ Masoud Sadrinasab
masoud.sadri@ut.ac.ir

Amir Reza Azarnivand
amirazarnivand@ut.ac.ir

Mohsen Nasseri
mnasseri@ut.ac.ir

[1] Faculty of Environment, University of Tehran, Tehran, Iran

[2] School of Civil Engineering, College of Engineering, University of Tehran, Tehran, Iran

capacity of seawater desalination (Lee and Kaihatu 2018), is a specific regional hotspot for climate change (Pal and Eltahir 2016) and brine discharge (Ibrahim et al. 2020). Asia's air temperature rising over the past four decades has been +0.35 °C per decade, twice the longer-term trend from 1910 to 2019 (NOAA's Global Climate Report for Annual 2019). Increases in air temperature and changes in precipitation patterns are considered to be critical climate change impacts for the Middle East (Salimi and Al-Ghamdi 2020). PG historically holds the highest sea surface temperature (SST) records in the world (Brandl et al. 2020), which is significantly affected by extremely high air temperatures associated with dry northwest and humid southeast winds (Paparella et al. 2019; Alosairi et al. 2020). Moreover, very high Gulf-wide averaged evaporation rates exceed the precipitation, creating hypersaline water and driving an inverse estuarine circulation (Al-Azri et al. 2014; Lorenz et al. 2020). These mounting values of temperature and salinity have already caused considerable degradation in the marine systems of PG (Riegl et al. 2018; Alosairi et al. 2020), and high rates of local extinction are projected by the end of the twenty-first century (Wabnitz et al. 2018; Buchanan et al. 2019). The WCPs in PG induce spatial variability in hydrographical characteristics, which in turn influence the chemical composition, pollution transport, and associated ecological processes in each water mass (Al-Said et al. 2018). Hence, it is crucial to understand how the effects of climate change on meteorological variables alter physical properties and affect the WCPs in PG.

Previous observations and numerical modeling studies on the physical properties of PG have shown that cyclonic circulation is driven by density differences, wind stress, tidal forcing, and freshwater fluxes (Ranjbar et al. 2020). The evolution of the exchange flow is predominantly density-driven (Moradi 2020) and follows a seasonal cycle, with a more vigorous exchange in spring and summer than in autumn and early winter (Yao and Johns 2010; Lorenz et al. 2020). Tidal forcing impacts circulation to a minor extent and only on the smaller scales of space and time (Campos et al. 2020). The salinity of PG is typically about 38–42 practical salinity units (psu) (Chow et al. 2019) and has been reported to be around 50 psu in limited areas (Anderlini et al. 1982; Lee and Kaihatu 2018), with considerable seasonal variation in temperature of below 20 °C in winter to above 35 °C in summer (Reynolds 1993; Alessi et al. 1999; Lorenz et al. 2020). A lower-saline Indian Ocean surface water (IOSW) flows into PG in the top layers, initially moving northward along the northern coast. The bulk of the flow mixes with the existing hypersaline water in PG (Johns et al. 2003; Chow et al. 2019; Campos et al. 2020). Dry northwesterly winds of 7 to 18 m/s, known as Shamal winds (Chow et al. 2019; Alosairi et al. 2020), occur first in the northwestern part of PG and then spread southeast behind the advancing cold front (Thoppil and Hogan 2010), create

an anti-cyclonic gyre along the northern coasts and a stronger cyclonic gyre along the southern coasts (Cavalcante et al. 2016; Ranjbar et al. 2020).

Extensive research has been conducted using hydrodynamic models to simulate current or past water mass properties of PG (e.g., Thoppil and Hogan 2010; Vasou et al. 2020). However, studies focusing on the future state of PG, specifically ones using the climate model products as input to the hydrodynamic models, are rare. The findings of these studies reveal increases in water temperature (e.g., Noori et al. 2019) and mixed rises and declines in salinity (e.g., Elhakeem and Elshorbagy 2015) in the future. Studies paying attention to the climate change impacts on the meteorological variables over the PG region primarily focus on wind fields and project a decreasing trend in future wind speeds (e.g., Alizadeh et al. 2020; Ranjbar et al. 2020; Wang et al. 2020). The meteorological condition of the surrounding land significantly influences the hydro-physical characteristics of PG (Noori et al. 2019; Alosairi et al. 2020). However, a detailed investigation into the future physical state of PG, considering the meteorological consequences of climate change on the surrounding land, has yet to be undertaken. Moreover, in previous studies, meteorological data have rarely been used in the daily resolution.

The main goal of this research is to explore how the interplay between climate change and meteorological variables influences salinity, temperature, and density of water mass concerning WCPs. The contribution of this paper is twofold: (a) To represent a perspective of meteorological conditions over the PG region at the beginning of the next decade, and (b) to project expected seasonal variations of PG hydrophysical properties in 2030. We chose the year 2030 due to the fact that the United Nations (UN) General Assembly (New York) has titled 2021–2030 the "UN Decade on Ecosystem Restoration" (Bennett 2019; Waltham et al. 2020). In this study, we simulated WCPs in PG for the beginning of the next decade under three climate change Representative Concentration Pathway (RCP) scenarios. To achieve this goal, we used the Statistical DownScaling Model (SDSM) to derive projected daily climate data. In addition, we once reran the hydrodynamic model with the same climatological inputs that Kämpf and Sadrinasab (2006) used in their already validated research conducted by the same model. This approach brings a valuable advantage of comparability of the results between these two studies.

Materials and Methods

Study Area

PG is a semi-enclosed sea in the Middle East, bordered by seven countries, Iran in the north and the United Arab

Emirates, Saudi Arabia, Qatar, Bahrain, Kuwait, and Iraq in the south and west, and geographically located between 47° 37′ E, 57° 57′ E, 23° 40′ N, and 30° 20′ N (Fig. 1a). With an average depth of 36 m and a maximum depth of 120 m, it is classified as a shallow water body. PG is connected to the Gulf of Oman, the Arabian Sea, and the Indian Ocean by the Strait of Hormuz (SoH) in the east. The annual mean outflow

transport of PG through SoH is about 0.25 Sv (Reynolds 1993; Johns et al. 2003; L'Hégaret et al. 2015). At the head of northwestern PG, the Arvandroud (also known as Shatt Al-Arab), which is a combined flow of the Euphrates, Tigris, and Karun rivers, provides the main freshwater inflow during the periods of rainfall in winter and melting of snow in spring (Al-Yamani et al. 2017). Air temperature in the region

Fig. 1 **a** The geographic features of the study area and bathymetry used in this study (orange arrows show schematic general WCP (Al-Azri et al. 2014; Xue and Eltahir 2015; Elobaid et al. 2022)), and **b** the locations of the meteorological stations and large-scale NCEP/ NCAR (and GCM) grid points (the grid points illustrating the centers of the grid boxes)
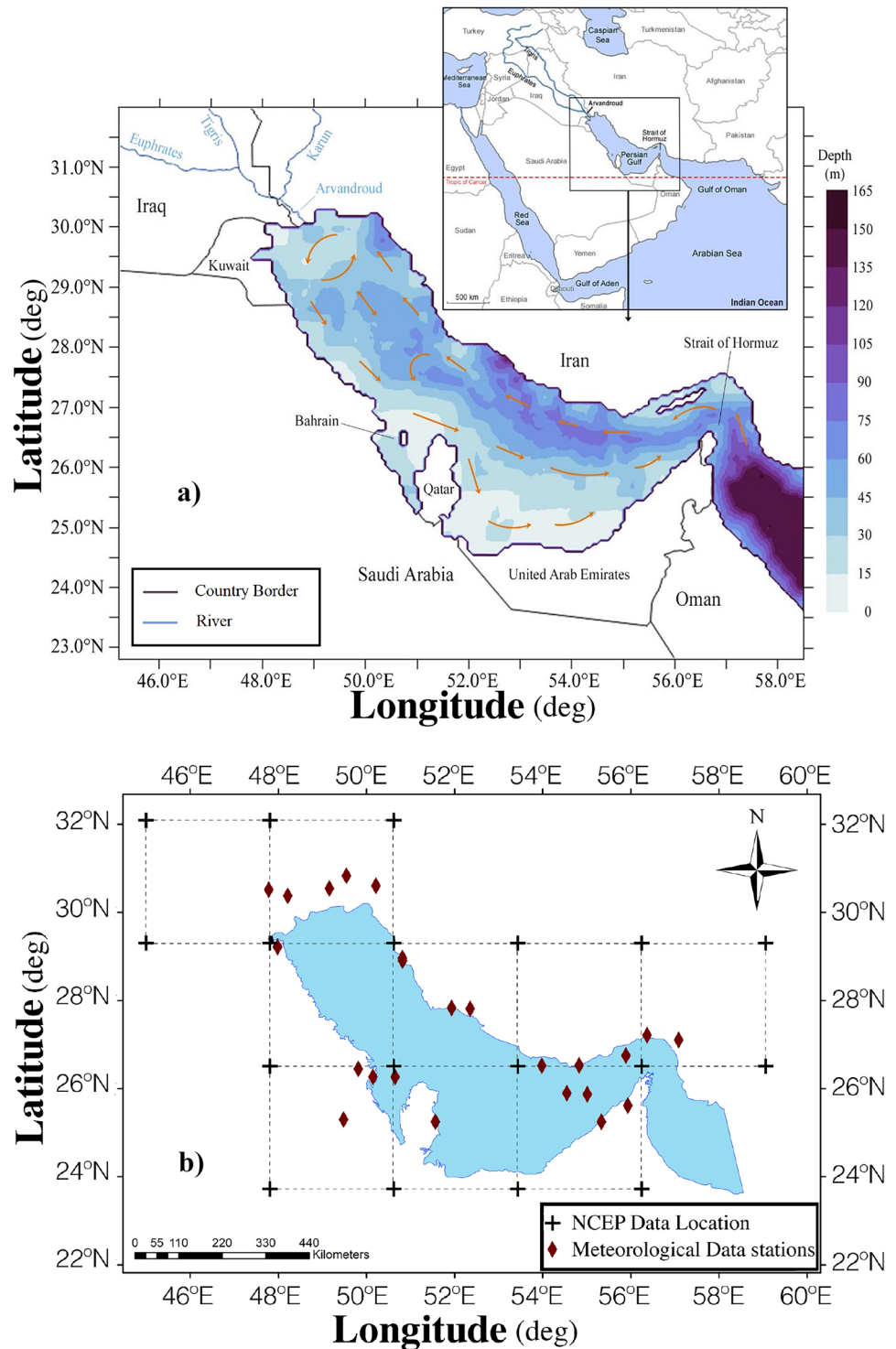
exceeds 50 °C in summer, and the mean annual rainfall along the southern and northern coasts is less than 50 and 200 mm, respectively (Noori et al. 2019).

Data Resources

To acquire a comprehensive view, we obtained long-term climatological data from 24 meteorological stations around PG on the coastline and the islands. Among these, 15 are located in Iran, and the others are scattered over other countries (Fig. 1b). According to the study's primary goal, we gathered data on the hydrodynamic model's meteorological inputs. These include cloud coverage, wind speed and direction, air temperature, precipitation, and relative humidity (from Basrah International Airport station, we could access only long-term air temperature data). Our most important criterion in station selection was the availability of observed meteorological data for more than 10 years.

The geographical location and length of the dataset in each station are demonstrated in Supplementary Table S1. As it shows, 10–45 years of daily records, ending in 2005, have been available for the stations in Iran and Iraq. For the other stations, we retrieved data from OGIMET (http://www.ogimet.com/gsynres.phtml.en), which provides daily data from 2000 to now. Insufficient data in these stations required a modification in the downscaling procedure. Depending on the data availability, each station's reference period differed from 10 to 45 years (1961–2005). We divided them into two sets: the first 75% of the data to calibrate the downscaling model and the rest for validation.

In this study, we downscaled the outputs of the second-generation Canadian Earth System Model (CanESM2), a very commonly-used general circulation model (GCM), for downscaling, especially by regression-based statistical approaches (e.g., Adham et al. 2019; Gebrechorkos et al. 2019), on the region. CanESM2 is one of the most well-known models producing daily predictor variables that can be directly applied to SDSM. The advantage of containing three RCP scenarios, RCP2.6 (a low concentration scenario), RCP4.5 (an intermediate concentration scenario), and RCP8.5 (a high concentration scenario), makes it appropriate to be used to project future climate conditions. We chose 18 GCM grid points covering the stations from datasets of CanESM2 (Fig. 1b) with a spatial resolution of 2.8125° (long.) × 2.8125° (lat.). Large-scale National Center for Environmental Prediction/National Center for Atmospheric Research (NCEP/NCAR) reanalysis atmospheric data with a spatial resolution of 2.5° (long.) × 2.5° (lat.) were interpolated onto the same grid as CanESM2 to be used as predictors. We derived the interpolated NCEP/NCAR data and CanESM2 daily simulations from Canadian Climate Data and Scenarios (CCDS). This database contains 26

atmospheric variables on each grid point from 1961 to 2005, listed in Supplementary Table S2. Among the stations, 19 could be surrounded by four-grid-point squares, and 5 stations could be covered by six-grid-point rectangles because these were located very close to the boundary of grid boxes (Supplementary Fig. S1).

We obtained bathymetry and coastline locations from the ETOPO-2 database (Fig. 1a). To prevent numerical instabilities, we slightly smoothed the bathymetry data onto a 4-min grid and eliminated local topographic irregularities, especially in SoH. Reaching an acceptable projection of the future changes in Arvandroud discharge needs independent research focusing on how climate change affects the quantity of water discharging throughout the river's catchment. Anthropogenic interference such as dam construction, the desiccation of the Mesopotamian marshlands, and the expansion of agricultural activities, in addition to the alterations in the rainfall patterns associated with climate change in the region, have reduced the river discharge (Alosairi et al. 2019). Nevertheless, extreme rain events have triggered high discharges persisting for several months (Alosairi et al. 2019). Limited access to hydrological data, especially about extreme rainfall events and the accompanying regional response to the high Arvandroud discharges, is a significant challenge hampering a reliable projection of the river discharge in the future (Bishop et al. 2011; Haghighi et al. 2020). Moreover, input from river discharge is much lower than estimates of evaporative flux, which is the determining factor in the Gulf-wide circulation in PG (Swift and Bower 2003). Hence, due to our target year for hydrodynamic simulation and our focus on alterations in meteorological conditions over the PG region, climate change impacts on river discharge and also on inflow from the open ocean are ignored in this research. We derived riverine and open ocean inflow properties from Kämpf and Sadrinasab (2006).

Model

We downscaled the CanESM2 datasets on the coastal stations and islands, and, after performance evaluation of the downscaling, we achieved daily values of the aforementioned meteorological variables for 2006–2100. We extracted the data for 2030 and interpolated them on a 4-min grid (similar to the bathymetry) by the inverse distance weighting (IDW) method, resulting in 5941 grid points of daily data. We divided these data into seasonal sets to demonstrate a long-term view of the future climatic condition over PG. Then, to be applicable to a uniform-in-space initialization, we used the arithmetic mean of these daily data as daily meteorological inputs of the hydrodynamic model.

Downscaling Model

Regression-based downscaling methods rely on empirical relationships between local predictands and regional predictors (Wilby et al. 2002). SDSM is developed based on a multiple linear regression downscaling model (Wilby et al. 2002) and assumes stable statistical relationships; that is, the empirical statistical relationship is constant in the case of future changes in climatic conditions (Wang et al. 2019). In this research, we utilized an open-source SDSM in the MATLAB environment for the downscaling purpose (Arfa and Nasseri 2019). SDSM outputs are the average of several weather ensembles that are the results of linear regression models improved by stochastic terms of bias correction. Because of the linear structure of SDSM, feature selection is usually handled through linear (and/or partial) correlation analysis between a predictand and its probable predictors, which are selected from NCEP/NCAR data. The weights of the predictors are calculated via simple least squares or dual simplex methods (Pahlavan et al. 2018). SDSM consists of a sub-model to simulate discrete meteorological variables (precipitation and cloud coverage in this study) and another for continuous variables (air temperature, relative humidity, and u- and v-components of wind speed in this study). It must be noticed that, in this research, we broke upwind speed into u- and v-components and then considered them as scalars. A detailed explanation of SDSM and its modules has been presented by Wilby et al. (1999, 2002), and the main steps of operating SDSM are briefly clarified in Pahlavan et al. (2018). (SDSM code in MATLAB is available at https://doi.org/10.5281/zenodo.7042148.)

The statistical performance of SDSM depends on selecting appropriate predictor variables while developing the predictor–predictand relationship because the choice of predictors determines the character of the downscaled climate scenario (Sada et al. 2019). In the current research, for each meteorological variable in each station, we analyzed 104 or 156 ($= 4$ or 6 (number of grid boxes) $\times$ 26 (atmospheric variables)) predictors. In the feature selection procedure, we used backward stepwise regression presented by Hessami et al. (2008).

As the historical period initially defined by the Coupled Model Intercomparison Project Phase 5 (CMIP5) ends in 2005 (Taylor et al. 2012), we calibrated SDSM with the NCEP/NCAR selected predictors until 2005. However, in this research, in 8 stations, observed data before 2000 have not been available, and 2000–2005 seemed too short to be confidently considered a reference period. In these stations, we calibrated the model with NCEP/NCAR reanalysis dataset for 2000–2016 or 2000–2017, depending on available observed data, on the same grid as GCM.

Performance Evaluation of Statistical Downscaling

Among various performance evaluation techniques available (e.g., Moriasi et al. 2007), we evaluated the performance of SDSM based on the coefficient of determination (R^2), root mean square error and normalized root mean square error (RMSE and NRMSE), Nash–Sutcliffe efficiency (NSE), Kling–Gupta efficiency (KGE), and Taylor skill score (TaylorSS) metrics. R^2 indicates a comparison between the simulated data's explained variance and the observed data's total variance and ranges from 0 to 1, with greater values showing less error variance. The RMSE is a widely used error metric measuring the difference between the observed and simulated values. It is commonly accepted that the lower the RMSE, the better the model performance (Moriasi et al. 2007). In this study, as the meteorological variables are of different units and scales (for example, cloud coverage is in okta and ranges between 0 to 8, but relative humidity is in percent and ranges between 0 to 100), we also normalized RMSE by the standard deviation of the observed values to be comparable and easy to interpret. The NSE is an often-used normalized statistic (e.g., Chitsaz et al. 2016) that determines the relative magnitude of the residual variance, or "noise," compared to the measured data variance, or "information" (Nash and Sutcliffe 1970). It provides an interpretable scale to evaluate the model's performance and indicates how well the plot of observed versus simulated data fits the 1:1 line (Moriasi et al. 2007). NSE ranges between $-\infty$ and its perfect value ($= 1$), where NSE $= 0$ indicates that the model simulations have the same explanatory power as the mean of the observations, and NSE < 0 indicates that the model is a worse predictor than the mean of the observations (Knoben et al. 2019). The KGE is based on a decomposition of NSE into its constitutive components (correlation, variability bias, and mean bias), addresses several perceived weaknesses in NSE (Gupta et al. 2009), and is increasingly used for model calibration and evaluation (e.g., Kling et al. 2012; Sada et al. 2019; Azarnivand et al. 2020). Same as NSE ranges between $-\infty$ and 1, where KGE $= 1$ indicates perfect agreement between simulations and observations, but KGE $> 1 - \sqrt{2} \approx -0.41$ is still considered to show "good" performance (Knoben et al. 2019). TaylorSS (Taylor 2001) is a commonly-used score in climate modeling studies (e.g., Ahmed et al. 2020; Khan et al. 2020; Tegegne et al. 2020) ranges between 0 for inverse model performance (when the correlation coefficient equals -1) and 1 for a perfect match (when r and σ equal 1) (Zamani and Berndtsson 2019). These metrics can be expressed as follows:

$$R^2 = \frac{\left[\sum_{i=1}^{N} (O_i - \overline{O})(P_i - \overline{P}) \right]^2}{\sum_{i=1}^{N} (O_i - \overline{O})^2 \sum_{i=1}^{N} (P_i - \overline{P})^2} \tag{1}$$

$$\text{RMSE} = \sqrt{\frac{\sum_{i=1}^{N}(O_i - P_i)^2}{N}} \tag{2}$$

$$\text{NRMSE} = \frac{\text{RMSE}}{\sigma_o} \tag{3}$$

$$N\text{SE} = 1 - \frac{\sum_{i=1}^{N}(O_i - P_i)^2}{\sum_{i=1}^{N}(O_i - \overline{O})^2} \tag{4}$$

$$\text{KGE} = 1 - \sqrt{(r-1)^2 + \left(\frac{\sigma_p}{\sigma_o} - 1\right)^2 + \left(\frac{\mu_p}{\mu_o} - 1\right)^2} \tag{5}$$

$$\text{TaylorSS} = \frac{4 \times (1 + r)}{\left(\frac{\sigma_p}{\sigma_o} + \frac{\sigma_o}{\sigma_p}\right)^2 \times (1 + r_0)} \tag{6}$$

where N is the length of time, O_i is the observed value, P_i is the simulated value, $\overline{O}$ is the mean of the observed values, $\overline{P}$ is the mean of the simulated values, r is the linear correlation between observations and simulations, r_0 is the maximum theoretical correlation (= 1.0 in this study), σ_o is the standard deviation in observed values, σ_p is the standard deviation in simulated values, μ_o is the observation mean (i.e., equivalent to $\overline{O}$), and μ_p is the simulation mean (i.e., equivalent to $\overline{P}$). In this research, we calculated and presented these performance criteria in the calibration and validation periods for each of the six aforementioned variables.

Hydrodynamic Model

To simulate the seasonal WCPs, we employed the hydrodynamic component of the COHERENS model (COupled Hydrodynamical-Ecological model for REgioNal Shelf seas) (Luyten et al. 1999), which uses terrain-following (sigma) coordinates. COHERENS is based on the Navier–Stokes equations that consist of the equations of momentum, continuity, temperature, and salinity, with the Boussinesq approximation involved in the horizontal momentum equations, and the model equations are solved on an Arakawa C-grid (Arakawa and Suarez 1983). The model is initialized in spatially uniform mode with Cartesian lateral coordinates on the f-plane (uniform Coriolis frequency) using a geographical latitude of 27° N. Hydrodynamic basis and formulation in sigma coordinates can be found in Luyten et al. (1999).

Since the current study mainly aims to assess the future physical state of PG under the altered meteorological state affected by climate change, comparing the results with the past or present state is beneficial. According to the lack of recently observed measurements in PG, hydrodynamic model validation

is problematic. We decided to set up COHERENS in the way presented in Kämpf and Sadrinasab (2006), which has already been validated by Alessi et al. (1999). The initial and boundary conditions and the numerical, mixing, and turbulence schemes used in the model are summarized in Supplementary Materials - A. Hydrodynamic model set-up. To briefly describe the lateral boundaries, at the eastern open ocean boundary, we considered 2-layer temperature and salinity profiles extracted from hydrographic observations (Alessi et al. 1999). The values of the upper layer differed monthly (Supplementary Table A1), and the water column underneath was kept at a temperature of 22 °C and a salinity of 36.5 psu throughout the previous simulations. River discharge varies in a sinusoidal mode with an annual mean of 500 m³/s (15.8 km³/year). We selected a minimum water depth of 3 m and, according to the model domain, limited the maximum water depth to 150 m, which applies only to the Gulf of Oman and does not affect the results notably. We employed a Cartesian lateral grid size of $\Delta x = 7.4$ km (east–west direction) and $\Delta y = 6.6$ km (north–south direction) and five sigma levels. We once forced COHERENS in daily mode by climatologic monthly mean atmospheric forcing derived from 54 years (1948–2002) of National Oceanic and Atmospheric Administration (NOAA) data. In the next step, we ran the model by the daily values of those variables obtained from SDSM for 2030. As three scenarios were considered to assess the climate change impacts in 2030, we forced COHERENS for each scenario separately. To reach a steady state seasonal cycle of water mass characteristics in PG, we chose a simulation duration of 10 years (including the first 9 years as a warm-up period) for each of four cases, namely the reference model (presented in Kämpf and Sadrinasab (2006) and hereafter would be called the Historical State of PG (HS) as it refers to 1948–2002) and the results of RCPs (2.6, 4.5, and 8.5) for 2030. In this paper, results gained from the last year of the simulation period are presented.

Results

SDSM Performance Evaluation

In this study, to assess the performance of SDSM, we calculated R^2, TaylorSS, NSE, KGE, and NRMSE statistics for each of the six meteorological variables (Fig. 2). The most significant values of R^2 (0.91–0.98), TaylorSS (0.97–0.99), NSE (0.91–0.98), and KGE (0.93–0.99) and the least values of NRMSE (0.16–0.29, refers to RMSE values between 0.99 and 2.12) of air temperature for both calibration and validation periods obviously demonstrated the paramount reliability of simulated daily air temperatures in SDSM. Although the results gained for all six variables revealed fair values, the statistics showed less accuracy in simulated precipitation with the largest NRMSE (mostly between 0.70 and 0.90, refers to

Fig. 2 Box-and-whisker plots of assessment metrics for SDSM in downscaling different meteorological variables for the calibration and validation periods; R2 (**a**), TaylorSS (**b**), NSE (**c**), KGE (**d**), and NRMSE (**e**)
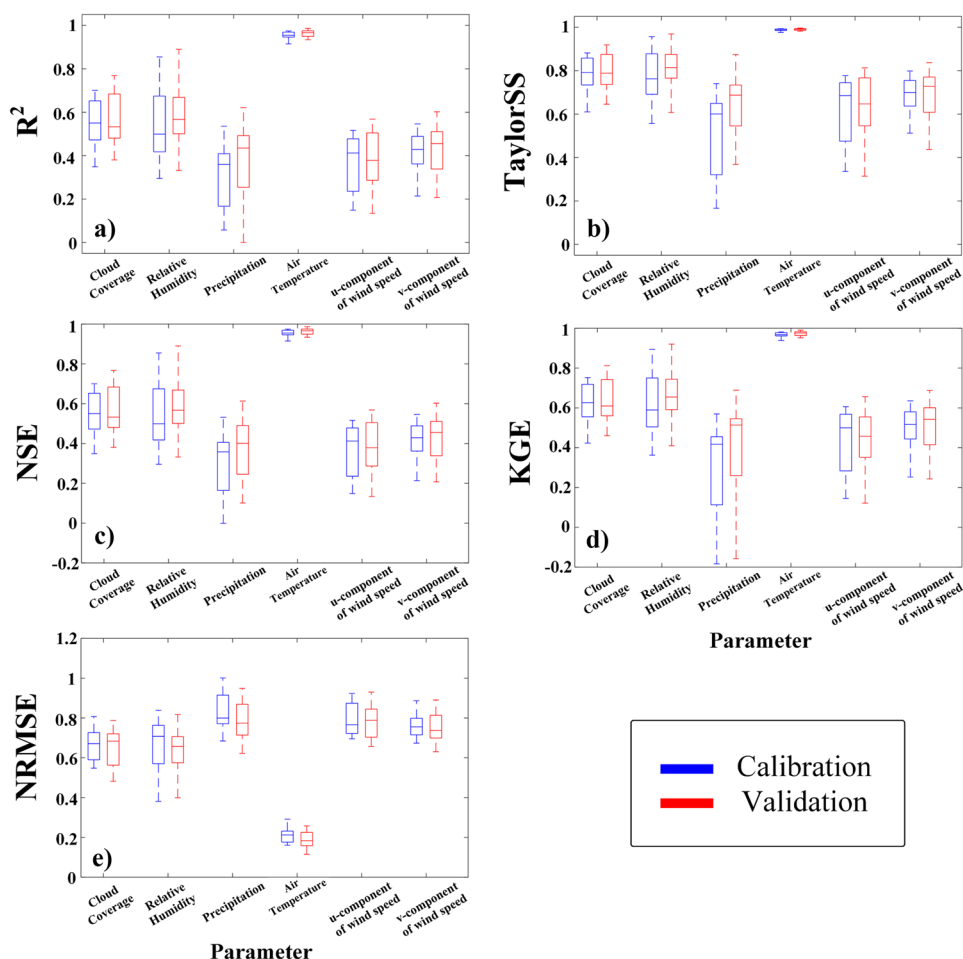
RMSE values between 1.67 and 2.94) and the smallest R^2 (mostly between 0.23 and 0.52), TaylorSS (0.04–0.87), NSE (0.07–0.53), and KGE (−0.18 to 0.69) for both the calibration and validation periods. Among the other variables, the performance of SDSM for cloud coverage and relative humidity was more satisfactory compared to wind speed components. The results indicated that SDSM shows its best performance in air temperature downscaling, while precipitation downscaling, due to its inherent high stochasticity, shows more uncertainty than the other five aforementioned variables.

The assessment of the climate change impacts on the selected meteorological variables under the three RCPs is presented in Supplementary Materials - C. Projected future climate.

The Persian Gulf Water Properties in the Future

Due to the tremendous amount of future data, assessment and representation of the meteorological properties in the region and hydrodynamic simulation for the entire period were challenging endeavors. Hence, the results are represented and discussed only for the beginning of the next decade. Before starting the hydrodynamic simulation, we interpolated the data of 2030 on a 4-min gridded area of PG by the IDW method and achieved 365 maps per scenario, covering the whole year of 2030.

Meteorological Properties

As the exchange flow in PG follows a seasonal cycle (Kämpf and Sadrinasab 2006; Pous et al. 2015), we separated the data into seasonal sets to represent a perspective of the meteorological state in different seasons in 2030. The average values in summer are graphically demonstrated on the maps in Fig. 3. In summer 2030, the eastern region of PG (between Qatar and SoH) experiences higher cloud coverage, relative humidity, and precipitation with lower air temperature and wind speed than the western half. This spatial pattern is not stable in the other seasons. In winter, higher cloud coverage and lower air temperature can be seen in the western region, and greater precipitation and relative humidity pertain to the central part of the northern coastline. In all seasons, the wind speed slows while moving eastward.
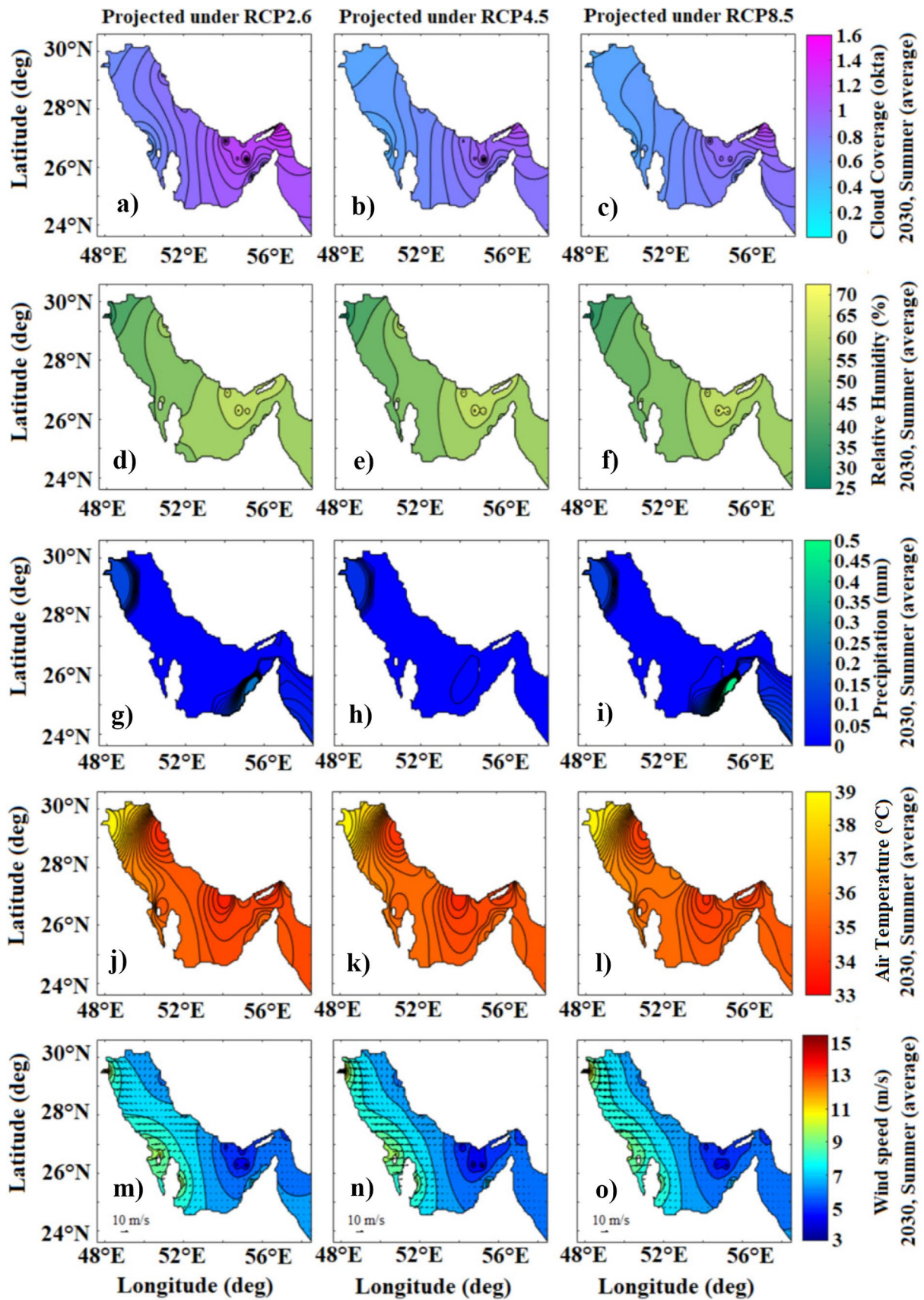
◀**Fig. 3** Spatial distributions of cloud coverage (**a–c**), relative humidity (**d–f**), precipitation (**g–i**), air temperature (**j–l**), and wind speed and direction (**m–o**) according to each scenario averaged for summer 2030, obtained on 23 (and 24 for air temperature) points and interpolated on a 4-min gridded area

The maps showing seasonal averages are available in Supplementary Figs. S11–S13.

The intensity of the impact of each scenario on each variable in various seasons is compared and shown in Fig. 4. According to this figure, in summer, projection under RCP2.6 shows greater values of cloud coverage, relative humidity, and wind speed compared to the other considered scenarios. In contrast, in winter, the most significant cloud coverage and relative humidity values belong to RCP4.5. By averaging the interpolated results in the seasonal sets, there is no regular relation to assessing scenarios' mutual severity or mildness.

Patterns of Water Temperature, Salinity, and Density in the Target Year

The interpolated data of 2030 in daily resolution showed minor standard deviations. The distribution and the average values of standard deviations are represented in Supplementary Table S3. These standard deviations indicate that the values for each day on the interpolated grid were very close to their arithmetic mean. Thus, due to the time and equipment limitations, we chose daily mean values in the spatially uniform initialization mode of COHERENS. After running the model as previously explained in the "Hydrodynamic Model" Section, we extracted seasonally-separated Gulf-averaged water temperature, salinity, and density on the bottom and surface layers to be shown as the primary physical characteristics determining WCP in PG. Note that HS refers to 1948–2002.

The variations of temperature, salinity, and density of water mass under the considered RCPs for 2030 in comparison to HS, 3D-averaged on a box named Central Region (CR) located between 51° 24′ E, 52° 9′ E, 26° 22′ N, and 27° 49′ N, are demonstrated in Fig. 5. The CR-averaged temperature of HS differs between 20.1 °C in January and February and 28 °C in August (Fig. 5b). In 2030, although the temperature follows the same curve, it shifts upward by approximately 4 °C, and the variation domain is between 23.5 and 32.6 °C. While the curves of scenarios move close to each other, RCP8.5 (between 23.5 and 31.8 °C) shows the closest values to HS, and RCP2.6 (between 24.2 and 32.6 °C) shows the warmest situation.

The CR-averaged salinity attains minimum values (≈ 40.1 psu) during July, and maximum salinities (≈ 40.8 psu) occur during September and October (Fig. 5c). RCPs show an increase in CR-averaged salinity in 2030. Like the

temperature graph, RCP8.5 (between 40.7 and 41.6 psu) and RCP2.6 (between 41.3 and 42.6 psu) show the least and the most increases in salinity, respectively.

Temperature and salinity are two main factors influencing water density which diminishes with salinity decline or temperature rise. The CR-averaged density reaches the maximum (≈ 1028.8 kg/m³) during February and March when the temperature is near its minimum, and the minimum values of density (≈ 1026.5 kg/m³) are in July and August when temperature maximizes and salinity is close to its minimum (Fig. 5d). The results clearly show a density decrease in 2030, with the highest and lowest intensity under RCP8.5 (between 1025.5 and 1028.2 kg/m³) and RCP2.6 (between 1026.1 and 1028.7 kg/m³), in succession.

Seasonal Variations of the Water Body Characteristics in the Target Year

The seasonal Gulf-wide variations of temperature, salinity, density, and current speed of the water body in 2030 and their differences with HS (it must be noted that HS refers to 1948–2002 and it is considered the historical state of the PG) can give a proper perspective of the climate change impacts (Alizadeh et al. 2020). Hence, we categorized the results to represent the seasonal distribution of the parameters above on the upper and lower sigma levels (surface and bottom) of PG. The maps showing the distributions of temperature, salinity, density, and current speed on the surface layer for summer are presented here, and the others are in Supplementary Figs. S14–S51. The distributions of surface net heat and salinity flux are also shown in Supplementary Materials to better understand the changes in temperature and salinity.

In summer, on the surface layer, as seen in Fig. 6, the whole water body becomes warmer under climate change compared to HS. However, RCP2.6 (Fig. 6d) shows the mildest (around 5 °C), and RCP8.5 (Fig. 6f) reveals the most severe (about 5.8 °C) rise in comparison to HS. In the RCPs, the bottom and surface layers become warmer than HS, except for a small area in the middle of SoH. On the bottom, in the southern part, RCP4.5 is the harshest scenario, with a nearly 9.5 °C increase relative to HS on the right side of Qatar. Still, in the northern region, RCP2.6 shows a more considerable rise in water temperature. RCP8.5 shows lighter differences with HS compared to the other two scenarios. In spring, an approximately uniform 7 °C rise on the surface (Supplementary Fig. S19) and nearly 8 °C in the southern region of the bottom layer (Supplementary Fig. S20) can be observed under RCP2.6 and RCP4.5. In autumn and winter (Supplementary Figs. S15–S18), the temperature rise is from 2 to about 5 °C, and RCP8.5 becomes the most severe scenario, especially on the surface. Details are represented graphically in Supplementary

Fig. 4 Seasonal comparison between the interpolated results under RCP scenarios for cloud coverage (**a**), relative humidity (**b**), precipitation in the western and eastern regions of PG (**c** and **d**), air temperature (**e**), and wind speed (**f**) in 2030
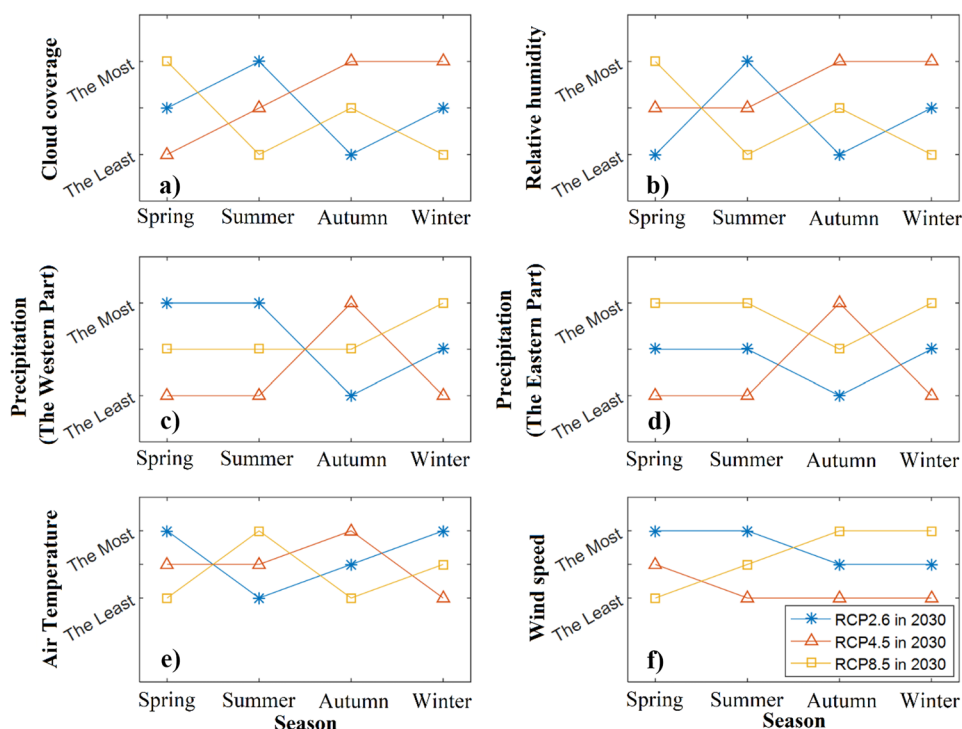
Figs. S14–S20. To check the results and achieve a mechanistic understanding of the temperature changes, we provided surface net heat flux for the whole year and each season in Supplementary Figs. S21–25.

Climate change results show similarities in the general pattern of salinity distribution (Fig. 7), with higher salinities in vast areas and lower on the surface of a box on the right side of Qatar in summer. In summer, RCP2.6 (Fig. 7d) and RCP8.5 (Fig. 7f) show the greatest and the lightest changes in salinity values, and this is generally true for the other seasons, as seen in Supplementary Figs. S26–S32. The results illustrate a decline in scattered, in some cases extensive, areas on the bottom layer in autumn and winter

(Supplementary Figs. S28 and S30) and on the surface layer in spring (Supplementary Fig. S31) and summer (Fig. 7) in 2030. The surface salinity flux for the whole year and each season is depicted in Supplementary Figs. S33–S37 to provide a better understanding of the changes in salinity.

The distributions of water density on the surface layer in summer show that the density of PG reaches its minimum in summer (Fig. 8) as the temperature rises and attains its maximum in winter (Supplementary Fig. 41) when the salinity is high and the temperature is low. The same cycle is perceived in RCPs for 2030, with an obvious decrease in almost the whole area of PG (except in autumn) relative to HS. Under RCP2.6 and RCP4.5, on some parts of the

Fig. 5 The location of the CR box (**a**) and the time series of temperature (**b**), salinity (**c**), and density (**d**) for last year's run of HS and each RCPs of 2030 simulations, averaged on the CR box
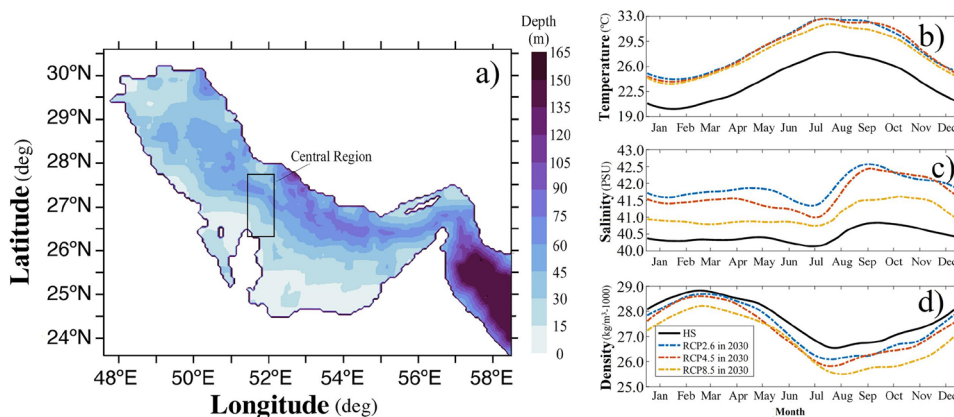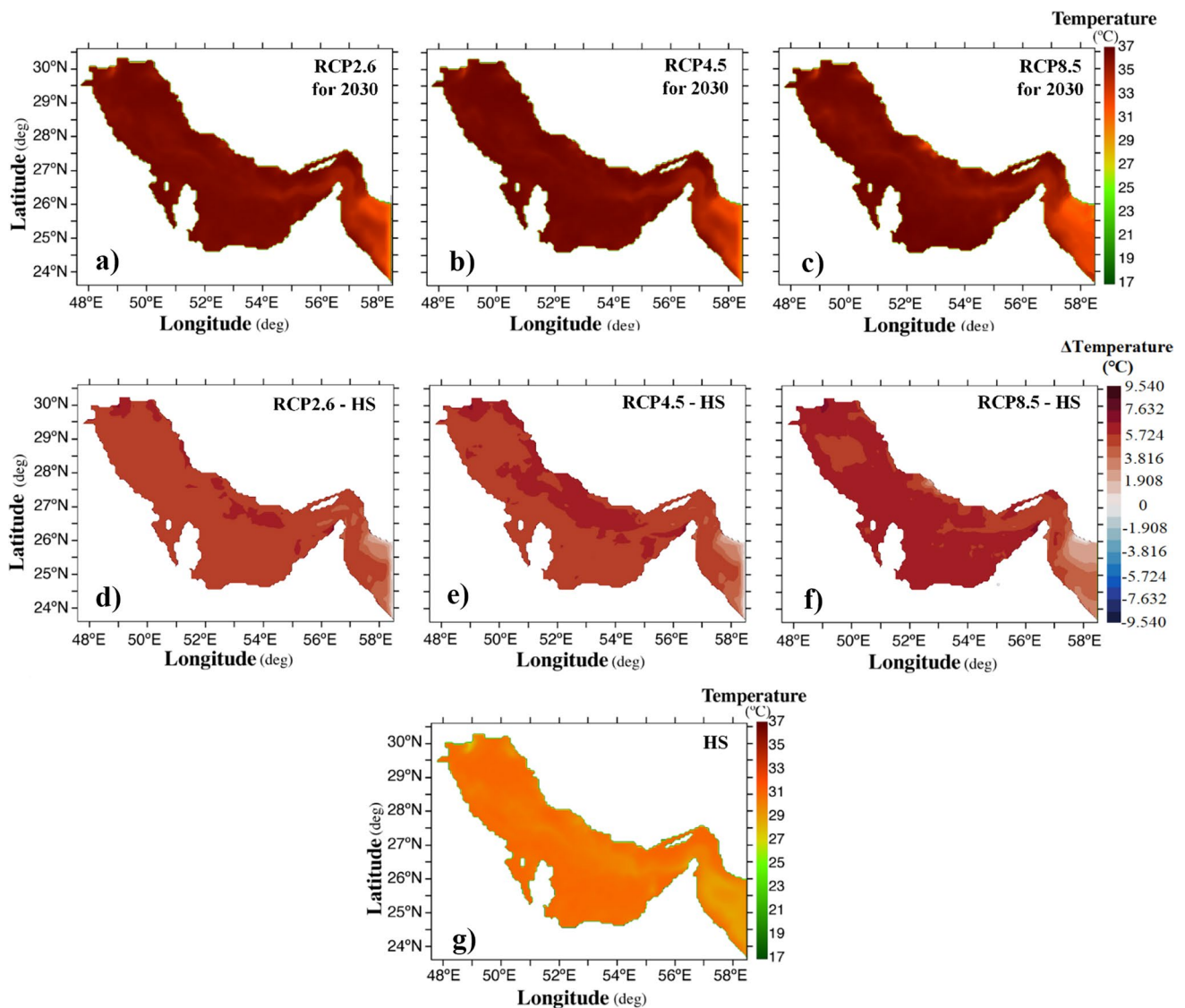
Fig. 6 Spatial distributions of water temperature on the surface layer averaged over summer for RCP 2.6 (**a**), RCP 4.5 (**b**), and RCP 8.5 (**c**) in 2030. Differences between water temperature distributions of each scenario and HS for RCP 2.6 (**d**), RCP 4.5 (**e**), and RCP 8.5 (**f**) show an obvious increase in temperature. HS is represented in (**g**)

surface layer in spring (Supplementary Fig. 43), the difference reaches -3.5 kg/m^3. In autumn and winter, RCP8.5 shows the most considerable difference in density with HS, while RCP2.6 and RCP4.5 demonstrate a low increase in autumn. RCP8.5 is the mildest scenario in warmer seasons, and the harshest differences occur under RCP4.5. Also, we should mention that the surface layer experiences more significant changes than the bottom layer. The distributions of density for the other seasons and the bottom layer in summer can be found in Supplementary Figs. S38–S44.

Current vectors demonstrating the speed and direction of water flow in PG are displayed over the speed magnitude in Fig. 9 for the surface layer in summer. On the surface, in relation to vertical density gradients, RCPs show very similar performances, with higher current speeds than HS in most parts. As low-density bonds near the northern coastline widen in summer and autumn under RCPs relative to HS, the strip formed by the IOSW becomes wider and stronger. However, on the dense bottom layer, a comparison between the results of RCPs in 2030 and HS shows almost no significant changes in the current speeds and directions. Current vectors are presented in Supplementary Figs. S45–S51 for the other seasons and the bottom layer in summer.
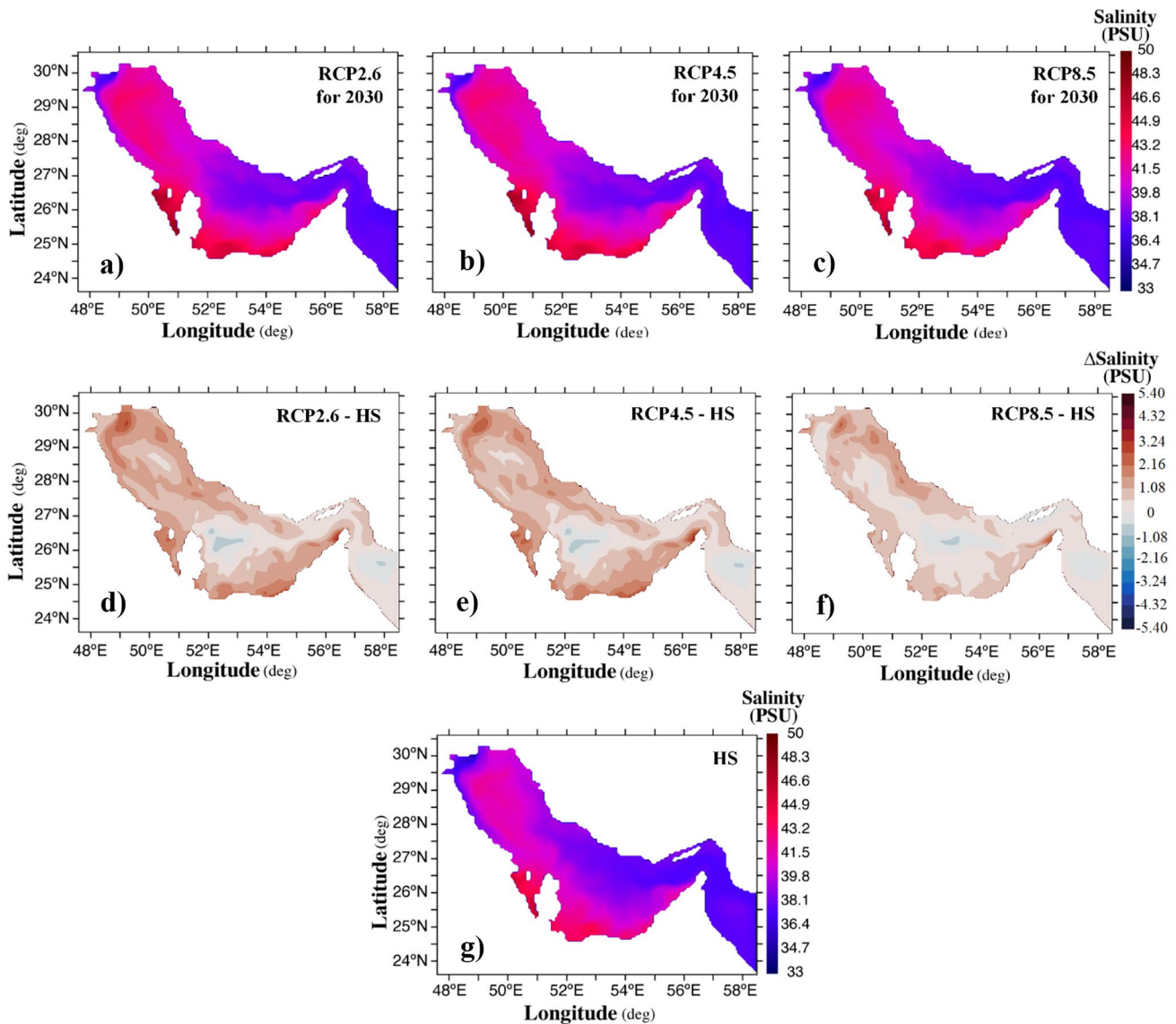
Fig. 7 Spatial distributions of water salinity on the surface layer averaged over summer for RCP 2.6 (**a**), RCP 4.5 (**b**), and RCP 8.5 (**c**) in 2030. Differences between water salinity distributions of each scenario and HS for RCP 2.6 (**d**), RCP 4.5 (**e**), and RCP 8.5 (**f**) show small positive values in most parts. HS is represented in (**g**)

Discussion

Climate Projections Over the Persian Gulf Region

We downscaled GCM data of six meteorological variables and achieved acceptable downscaling performance for all of them. However, various metrics used in this study to evaluate the performance of SDSM reveal its relative weakness in downscaling precipitation. Precipitation time series have stochastic nature and high variation, specifically in semi-arid and arid regions, which leads to downscaling precipitation with lower accuracy (Anaraki et al. 2021). It has been shown that, in such regions, SDSM represents weaker performance for precipitation downscaling than regions with higher precipitation rates (e.g., Liu et al. 2011; Wilby and Dawson 2013; Wang et al. 2019). A reason could be the small number of non-zero observed values in such regions, which restricts the quality of linear regression. It is becoming increasingly apparent that climate change modeling in arid zones is extremely uncertain, partly because of the extreme natural spatiotemporal variability of the desert climate and partly because of inherent uncertainties in global and regional climate modeling (Lioubimtseva and Cole 2006). Gaur et al. (2021) obtained sound performance for temperature and believed that climate models often fail to represent the statistical
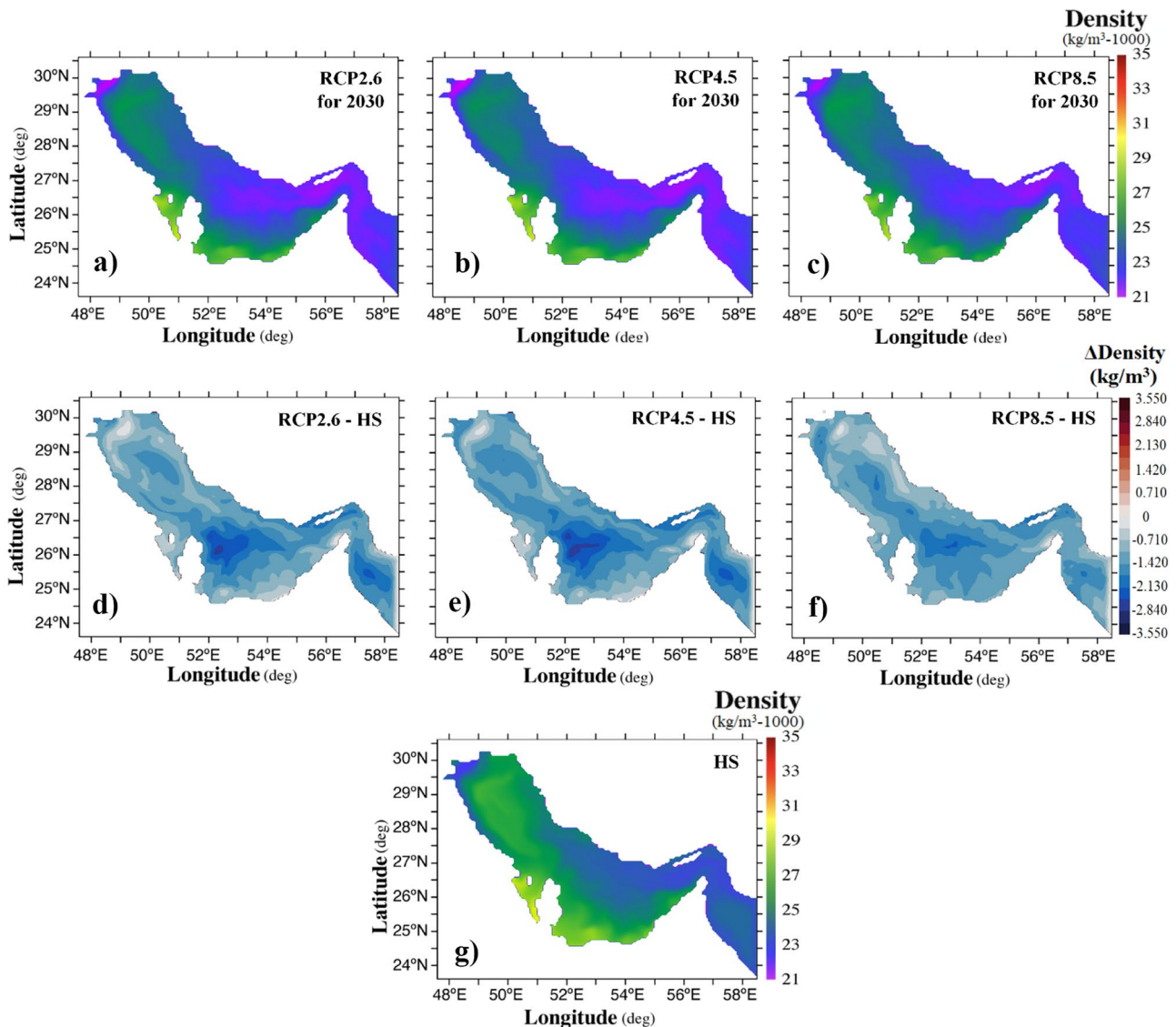
Fig. 8 Spatial distributions of water density on the surface layer averaged over summer for RCP 2.6 (**a**), RCP 4.5 (**b**), and RCP 8.5 (**c**) in 2030. Differences between water density distributions of each scenario and HS for RCP 2.6 (**d**), RCP 4.5 (**e**), and RCP 8.5 (**f**) show a decrease in water density. HS is represented in (**g**)

properties of observed climate variables such as precipitation. Precipitation is not only affected by atmospheric circulation factors but also by the underlying surface conditions and human activities, thereby hindering its accurate projection (Wang et al. 2019).

Our findings on the projected future meteorological condition of the region are consistent with many other regional climate change studies (e.g., AlSarmi and Washington 2011; Elhakeem et al. 2015; Al-Mukhtar and Qasim 2019; Alizadeh et al. 2020; Wang et al. 2020), which reported an increase in air temperature and a decrease in precipitation and wind speed during the subsequent decades in different parts of the study area. Although our wind field results

are in line with several studies (e.g., Alizadeh et al. 2020; Wang et al. 2020), Ranjbar et al. (2020) found alterations in wind direction, which might be due to different approaches and different data they used. Because employed GCMs, selected predictors, and downscaling methods highly affect the results of downscaling, assessing climate projections in diverse climates using various downscaling schemes has presented contradictory results (Baghanam et al. 2020). Differences in GCMs and downscaling approaches are two major sources of uncertainties in climate change assessments that cause significant differences in downscaled outcomes. Downscaling methods can alter fundamental climate change signals (Liu et al. 2017). The performances of various GCMs
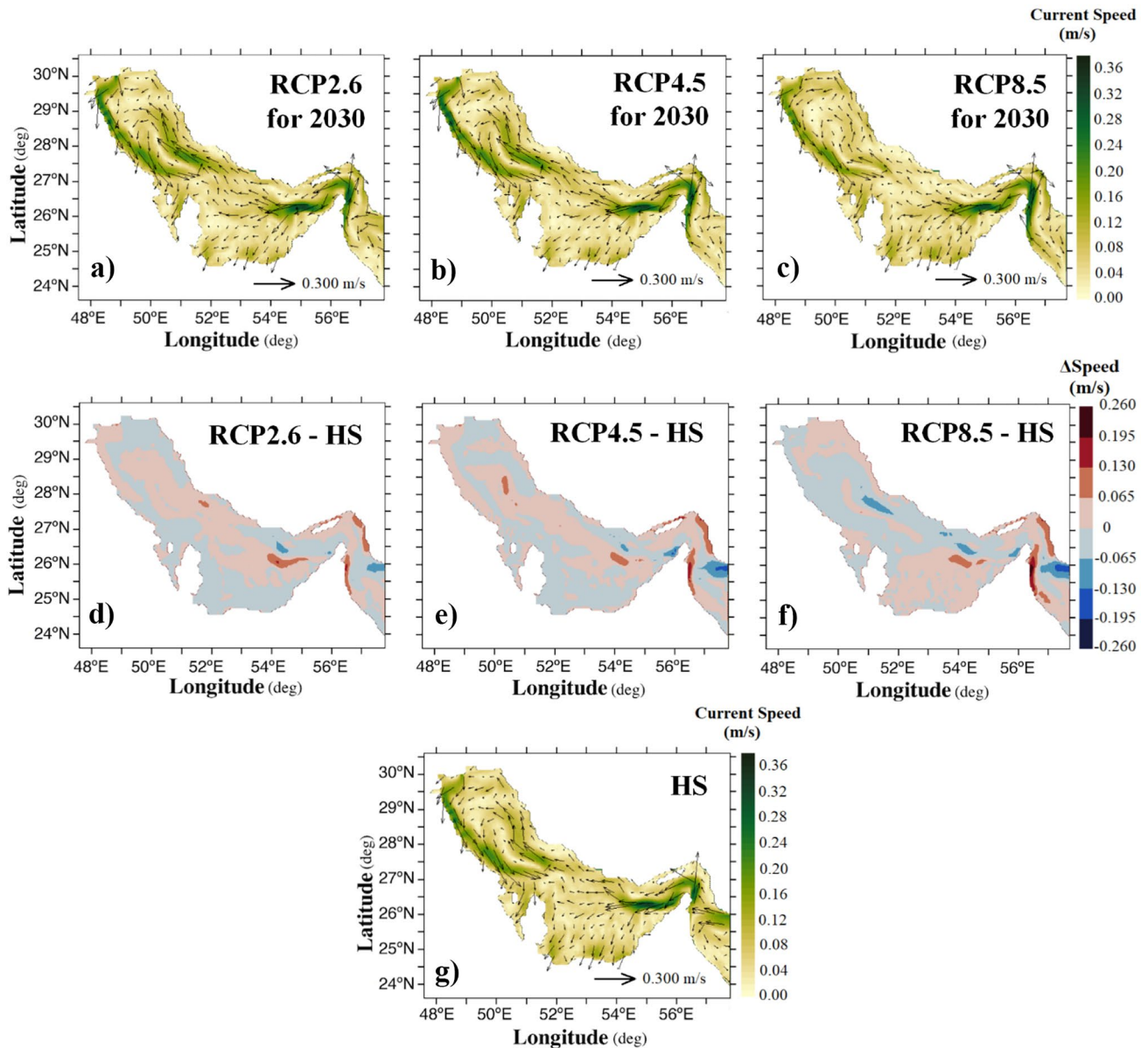
Fig. 9 Spatial distributions of current vectors over speed on the surface layer averaged over summer for RCP 2.6 (**a**), RCP 4.5 (**b**), and RCP 8.5 (**c**) in 2030. Differences between the current speed distributions of each scenario and HS for RCP 2.6 (**d**), RCP 4.5 (**e**), and RCP 8.5 (**f**) show an increase in current speed in vast areas. HS is represented in (**g**)

have been shown to vary over different regions (Ahmed et al. 2019). Of course, different downscaled results among GCMs are not surprising, as the GCMs are developed based on various assumptions, approximations, and parameterizations (Rashid et al. 2015).

General Water Circulation Patterns in the Persian Gulf

Changes in meteorological variables directly influence the evaporation rate and exchange flow, which noticeably

affects hydro-physical properties. In PG, the general WCP follows a seasonal cycle, and water exchange and circulation interact closely with water temperature, salinity, and density.

Our simulation shows that in summer, a cyclonic overturning circulation is formed along the length of PG (Fig. 9g). The IOSW reclines on the northern coastline with a prominent effect on the bottom layer and, at the northwestern head, merges with Arvandroud inflow. The combined flow is pushed to the south along the Arabian coast by steady northwesterly wind until reaching around

Bahrain and Qatar. In the center of the northwestern part, a denser, enclosed inert region initiates with an overall counter-clockwise gyre around. In 2030, the density gradients increase, and the surface currents' speeds rise, mostly under RCP2.6 (Fig. 9a) and RCP4.5 (Fig. 9b). Moreover, the area of the enclosed inert region diminishes slightly. On the bottom layer with almost uniform densities, dense water moves eastward to leave PG from SoH (Supplementary Fig. S45). In autumn, the IOSW zigzags and does not reach Arvandroud inflow, and, in a more chaotic pattern, the cyclonic circulation is not formed (Supplementary Fig. S46). The lower temperature in autumn makes the bottom water denser, and relatively lower densities of the bottom layer under RCP8.5 produce slower bottom currents compared to the other scenarios (Supplementary Fig. S47). In winter, the IOSW has broken up into mesoscale eddies on the surface layer, producing turbulence and vanishing Arvandroud inflow (Supplementary Fig. S48). Hence, a very turbulent pattern on the surface layer in winter is also distinguishable among the considered scenarios. The directions of current vectors are not similar in RCPs. Cooler high-saline water in winter causes higher densities on the bottom layer (Supplementary Fig. S49). Spring is the time when the strong IOSW forms as a consequence of strong density gradients across SoH. In spring, the Arvandroud plume can be distinguished, and the IOSW vanishes the mesoscale eddies (Supplementary Fig. S50).

The general WCP of HS is identifiable under RCPs for 2030, which seems inconsistent with the findings of Ranjbar et al. (2020). They indicated that although sea level rise will not change the general WCP in PG, the changes in the future wind field will alter both the speed and the direction of residual currents. The inconsistency comes from the different projected wind fields in the two studies. Altered wind directions in Ranjbar et al. (2020) have resulted in altered direction of residual currents.

Water Temperature and Salinity of the Persian Gulf

Due to nonlinear relationships among variables, water temperature and salinity modeling are complex procedures. In oceans and gulfs, where tidal and wind waves affect surface waters, the complexity of the problem is further exacerbated (Shamshirband et al. 2019). It is not possible to accurately compare the CR-averaged variations of temperature, salinity, and density in 2030 (Fig. 5) with the other studies. However, the decreasing pattern of salinity (on the CR box) and rising pattern of temperature that Elhakeem and Elshorbagy (2015) presented corroborate our results, and the temperatures are roughly in accord with Noori et al. (2019). As the model has been validated by Alessi et al. (1999), the temperature and salinity values of HS are consistent with the observations.

Generally, the results reveal a temperature rise in all seasons in 2030. In the warmer seasons, summer and spring, larger increases occur. Summer is highly linked to climatic effects (Alosairi and Pokavanich 2017). The differences between each scenario and HS on the surface in summer seem semi-uniform but with little lower values near SoH. On the bottom layer, in summer (Supplementary Fig. S14), there is a significant difference of about 11 °C between the cooler northern half and the warmer southern part of PG in the RCPs. According to the bathymetry of PG, the north region is much deeper than the southern part, and vertical temperature gradients in the shallower south are smaller. Thus, the bottom temperature in the shallower southern part is close to the surface temperature. As Al-Yamani et al. (2017)'s results of long-term monitoring of the hydrographic conditions in the northwest of PG over the last three decades showed, an average summer SST of nearly 37 °C is not surprising in PG. Alosairi et al. (2020) in-situ SST measurements for five consecutive years (2016, 2017, 2018, 2019, and 2020) indicated similar temperatures as well, of course in the northwest of PG. Top-to-bottom temperature gradients reach more than 10 °C in HS and exceed 12 °C in 2030. This is in agreement with the measurements first time conducted by Emery (1956), showing summer thermocline in PG.

The distributions of salinity on the surface of PG in summer (Fig. 7) show the low-saline robust inflow of IOSW makes a wide low-saline strip in the northeast. Also, the low-saline inflow of Arvandroud forms a narrow low-saline strip on the surface layer in the southwest. On the southern coastline, there is a restricted region with high amounts of salinity. In spring and early summer, as the inflow of Arvandroud increases, the western low-saline surface strip becomes broader and more powerful, so the salinity values decrease more in that part. Under RCPs, in all seasons, salinity increases in most parts, especially in the restricted southern region.

Our findings in increasing water temperature patterns over PG, mostly in spring and summer, and slight changes, increasing in some parts and decreasing in others, of salinity under climate change impacts, and spatial distributions in HS are similar to that reported by the previous studies (e.g., Xue and Eltahir 2015; Elhakeem and Elshorbagy 2015; Al-Said et al. 2018; Noori et al. 2019). Elhakeem and Elshorbagy (2015) showed an increase in salinity in vast areas of PG, with a decline in some parts. Still, they reported more minor temperature changes compared to our study, which might be due to differences in scenarios, data, and methodology between the two studies. They considered A2 and B1 scenarios from the Special Report on Emissions Scenarios (SRES), which are not directly comparable to RCP scenarios (Clarke et al. 2014). They also used the outputs of MAGICC/SCENGEN (model for the assessment of greenhouse-gas

induced climate change/a regional climate SCENario GENerator) for 2020, 2050, and 2080 as inputs for the Delft3D-Flow hydrodynamic model. Furthermore, the meteorological aspect of their study was mainly focused on air temperature, and the other variables were extended to 2080 without change. Differences in methods and models with various assumptions and formulations can produce different results. Also, with a completely different methodology, Noori et al. (2019) showed an increasing pattern in the SST of PG.

Water exchange across SoH is forced mainly by extensive annual evaporation, which drives a shallow inflow of IOSW from the Arabian Sea and a deep outflow of dense hypersaline PG water (PGW) (Schott and McCreary, Jr. 2001; Vasou et al. 2020). Seasonal variations in the strength of IOSW influx predominantly contribute to altering physical properties and processes in PG. Significantly, the salinity variations in PG are strongly sensitive to the inflow of IOSW (Yao and Johns 2010), which is highly vulnerable to monsoon wind changes (Kämpf and Sadrinasab 2006) and is more effective in summer. In winter, when IOSW is weak, stronger winds and a more considerable difference between air and water temperature cause higher evaporation rates and, consequently, higher salinity. In this study, we focused on changes in meteorological variables over PG and assumed that climate change does not make IOSW warmer. Due to the tremendous volume of ocean water compared to PG, IOSW could be supposed as an infinite water reservoir with negligible variations in evaporation regime and meteorological variables under climate change impacts, particularly in the near future. In spite of being negligible, this assumption might have led to an underestimated rise in vertical density gradients. Increasing trends of surface salinity in the northwestern Indian Ocean and the Arabian Sea (Durack and Wijffels 2010; Trott et al. 2019) coupled with temperature rise results in IOSW inflow with lower density and different hydro-physical characteristics.

Effects on Biodiversity of the Persian Gulf

With a variety of habitats, including coral reefs, sabkhas, mudflats, mangrove swamps, and seagrass beds that play a significant role in carbon storage within this region (Campbell et al. 2015) and also can be rich in marine biodiversity, PG is a productive maritime region (Burt 2014). However, marine biodiversity is rapidly declining from the synergistic effects of increasing environmental extremes associated with climate change and extensive anthropogenic stressors (Buchanan et al. 2019).

More than 7000 km² of seagrasses in PG, with the world's second-largest population of dugongs and green turtles, play a vital role in stabilizing the nearshore seabed and as food for threatened species or indirect source of food for many marine organisms (Erftemeijer and Shuail 2012). Some studies in the United States have claimed that seagrasses are likely to benefit from climate change due to ocean acidification and more abundant carbon dioxide substrate (e.g., Zimmerman 2021). In contrast, Guerrero-Meseguer et al. (2020) did not observe any changes in the seagrass bed composition of the northern Gulf of Mexico in response to acidification. They mentioned the environmental changes in salinity and turbidity to be the significant factors counteracting any positive effects of ocean acidification. There are vast arid deserts in the south of PG, and the increasing frequency of dust storms in the region brings prodigious loads of nutrients to PG, which impacts its water quality and the equilibrium of its ecosystem (Al Azhar et al. 2016). Temperature is another factor affecting seagrass growth. According to Erftemeijer and Shuail (2012), seagrass species in PG can tolerate wide ranges of salinity and temperature (up to 37 °C). Thus, our salinity and temperature projections do not indicate a threatening condition for PG seagrasses in the near future.

The heat-tolerant PG coral populations, adapted to cope with exceptionally high seasonal temperature maxima and large annual fluctuations, represent a genetic resource that could potentially facilitate the necessary increases in thermal tolerance for corals to withstand temperatures projected towards the turn of the century (Hume et al. 2015). These corals are mainly found in coastal regions that, due to our projections, are becoming not only warmer but also saltier. A rise in temperature and salinity, especially in summer, could provide suitable conditions for some species of dinoflagellates that cause harmful algal blooms in the Gulf of Oman and PG (Al-Azri et al. 2014), threatening these and other remarkable habitats and species.

Alterations in water temperature, salinity, and density influence the physical and chemical conditions of the marine environment and impact the rich biodiversity of PG. Furthermore, any differentiations in these parameters can affect the Gulf of Oman and the open ocean through PGW, an oxygenated high-salinity water mass identifiable in the Arabian Sea (Phillips et al. 2021). PGW is one of the major factors causing harmful algal blooms in the Gulf of Oman (Sedigh Marvasti et al. 2016). Warmer PGW, as projected in our study, could lower its oxygen concentrations (Rixen et al. 2020) and alter the ventilation of the Arabian Sea oxygen minimum zone, leading to an increase in hypoxic and anoxic events in the northern Arabian Sea (Lachkar et al. 2019). This potentially has profound consequences for the biogeochemical and ecological functioning of the Arabian Sea and the Indian Ocean at large (Sheehan et al. 2020).

Conclusion

This study attempts to assess how the interplay between climate change and the meteorological variables affects salinity, temperature, and density of water mass in relation to WCPs in PG. We downscaled the required meteorological inputs of the hydrodynamic model, COHERENS, including cloud coverage, relative humidity, precipitation, air temperature, and wind speed components, using SDSM. Then, we projected water temperature, salinity, density, and WCP under three RCP (2.6, 4.5, and 8.5) scenarios for the target year 2030.

The meteorological state is significantly influenced by climate change and highly impacts water temperature and circulation in PG. According to this study, altered meteorological variables under the impacts of climate change, especially higher air temperature and less precipitation, at the beginning of the next decade will lead to higher water temperature, higher salinity (except on the surface of a box at the right side of Qatar), lower surface density, and larger vertical density gradients, which cause a rise in speeds of surface currents. A higher evaporation rate that results in greater water exchange (outflow of dense high-saline PGW and inflow of lower-saline IOSW) might be the leading cause. This effect of the phenomenon has been shown by Swift and Bower (2003) in detail. The general WCP of HS, including cyclonic overturning circulation in summer, meanders of the surface inflow from SoH in autumn, mesoscale eddies in winter, Arvandroud plume in spring, etc., can still be seen under RCPs in 2030.

Evaluating other GCMs and downscaling approaches is highly recommended to achieve a comprehensive perspective of climate change on PG in future studies. Perhaps combinations of different GCMs, especially from CMIP6 models and scenarios, could be assessed and used. According to climatic changes and the development of the desalination industry in the region, more and newer observational data are required to provide the possibility of more accurate model validation and obtain more precise results. The reliable, higher-resolution bathymetry data would lead to more accurate results. Variations in Arvandroud discharge and inflow salinity (especially due to the development of the desalination industry) and the effects of climate change on them are uncertainty sources in hydrodynamic simulation. It is recommended to consider these variations and effects in future studies. Modeling for a more extensive duration and focusing on heat flux forcing on the circulation in PG can help to obtain a more expansive view of climate change impacts on PG. Furthermore, the biological effects of the changing physical state of PG can be the focus of future studies.

The mounting values of temperature and salinity have resulted in extensive degradation in the marine ecosystems of PG like coral reefs during the recent decades (Riegl and Purkis 2015; Burt et al. 2019), and this study projects more severe degradations in the future. Since marine ecosystems represent significant biodiversity hotspots in this arid region (Vaughan et al. 2019), there are likely to be serious ecological depletions as a consequence of rising temperatures (Bouwmeester et al. 2020) and salinities (Elobaid et al. 2022). Alterations in temperature and salinity affect the physical and chemical state (e.g., pH) of PG, which directly influences algal growth (Deng et al. 2021). There will also be knock-on effects for fish, both as a result of loss of habitat as well as direct physiological costs from more extreme environmental conditions (Buchanan et al. 2016; D'Agostino et al. 2021).

Declarations

References

Adham, A., J.G. Wesseling, R. Abed, M. Riksen, M. Ouessar, and C.J. Ritsema. 2019. Assessing the impact of climate change on rainwater harvesting in the Oum Zessar watershed in Southeastern Tunisia. *Agricultural Water Management* 221: 131–140. https://doi.org/10.1016/j.agwat.2019.05.006.

Ahmed, K., D.A. Sachindra, S. Shahid, Z. Iqbal, N. Nawaz, and N. Khan. 2020. Multi-model ensemble predictions of precipitation and temperature using machine learning algorithms. *Atmospheric Research* 236: 104806. https://doi.org/10.1016/j.atmosres.2019.104806.

Ahmed, K., S. Shahid, N. Nawaz, and N. Khan. 2019. Modeling climate change impacts on precipitation in arid regions of Pakistan: A non-local model output statistics downscaling

approach. *Theoretical and Applied Climatology* 137 (1): 1347–1364. https://doi.org/10.1007/s00704-018-2672-5.

Al Azhar, M., M. Temimi, J. Zhao, and H. Ghedira. 2016. Modeling of circulation in the Arabian Gulf and the Sea of Oman: Skill assessment and seasonal thermohaline structure. *Journal of Geophysical Research: Oceans* 121 (3): 1700–1720. https://doi.org/10.1002/2015JC011038.

Al-Azri, A.R., S.A. Piontkovski, K.A. Al-Hashmi, J.I. Goes, H.D.R. Gomes, and P.M. Glibert. 2014. Mesoscale and nutrient conditions associated with the massive 2008 Cochlodinium polykrikoides bloom in the Sea of Oman/Arabian Gulf. *Estuaries and Coasts* 37 (2): 325–338. https://doi.org/10.1007/s12237-013-9693-1.

Alessi, C. A., H.D. Hunt, and A.S. Bower. 1999. *Hydrographic data from the US Naval Oceanographic Office: Persian Gulf, Southern Red Sea, and Arabian Sea 1923–1996*. Woods Hole Oceanographic Institution Technical Report. WHOI-99-02, p 70. https://doi.org/10.1575/1912/78.

Al-Mukhtar, M., and M. Qasim. 2019. Future predictions of precipitation and temperature in Iraq using the statistical downscaling model. *Arabian Journal of Geosciences* 12 (2): 25. https://doi.org/10.1007/s12517-018-4187-x.

Al-Said, T., T. Yamamoto, R. Madhusoodhanan, F. Al-Yamani, and T. Pokavanich. 2018. Summer hydrographic characteristics in the northern ROPME Sea Area: Role of ocean circulation and water masses. *Estuarine, Coastal and Shelf Science* 213: 18–27. https://doi.org/10.1016/j.ecss.2018.07.026.

AlSarmi, S., and R. Washington. 2011. Recent observed climate change over the Arabian Peninsula. *Journal of Geophysical Research: Atmospheres* 116 (D11). https://doi.org/10.1029/2010JD015459.

Al-Yamani, F., T. Yamamoto, T. Al-Said, and A. Alghunaim. 2017. Dynamic hydrographic variations in northwestern Arabian Gulf over the past three decades: Temporal shifts and trends derived from long-term monitoring data. *Marine Pollution Bulletin* 122 (1–2): 488–499. https://doi.org/10.1016/j.marpolbul.2017.06.056.

Alizadeh, M.J., M.R. Kavianpour, B. Kamranzad, and A. Etemad-Shahidi. 2020. A distributed wind downscaling technique for wave climate modeling under future scenarios. *Ocean Modelling* 145: 101513. https://doi.org/10.1016/j.ocemod.2019.101513.

Alosairi, Y., N. Alsulaiman, P. Petrov, and Q. Karam. 2019. Responses of salinity and chlorophyll-a to extreme rainfall events in the northwest Arabian Gulf: Emphasis on Shatt Al-Arab. *Marine Pollution Bulletin* 149: 110564. https://doi.org/10.1016/j.marpolbul.2019.110564.

Alosairi, Y., N. Alsulaiman, A. Rashed, and D. Al-Houti. 2020. World record extreme sea surface temperatures in the northwestern Arabian/Persian Gulf verified by in situ measurements. *Marine Pollution Bulletin* 161: 111766. https://doi.org/10.1016/j.marpolbul.2020.111766.

Alosairi, Y., and T. Pokavanich. 2017. Seasonal circulation assessments of the northern Arabian/Persian Gulf. *Marine Pollution Bulletin* 116 (1–2): 270–290. https://doi.org/10.1016/j.marpolbul.2016.12.065.

Anaraki, M.V., S. Farzin, S.F. Mousavi, and H. Karami. 2021. Uncertainty analysis of climate change impacts on flood frequency by using hybrid machine learning methods. *Water Resources Management* 35 (1): 199–223. https://doi.org/10.1007/s11269-020-02719-w.

Anderlini, V.C., P.G. Jacob and J.W. Lee. 1982. Atlas of physical and chemical oceanographic characteristics of Kuwait Bay. *Kuwait Institute for Scientific Research, Report No. KISR* 704.

Arakawa, A., and M.J. Suarez. 1983. Vertical differencing of the primitive equations in sigma coordinates. *Monthly Weather Review* 111 (1): 34–45. https://doi.org/10.1175/1520-0493(1983)111%3C0034:VDOTPE%3E2.0.CO;2.

Arfa, S., and M. Nasseri. 2019. Assessment of single site versus multisite downscaling methods on estimation of rainfall extreme values. *Journal of the Earth and Space Physics* 45 (3): 575–597. https://doi.org/10.22059/jesphys.2019.274469.1007083.

Azarnivand, A., M. Camporese, S. Alaghmand, and E. Daly. 2020. Simulated response of an intermittent stream to rainfall frequency patterns. *Hydrological Processes* 34 (3): 615–632. https://doi.org/10.1002/hyp.13610.

Baghanam, A.H., M. Eslahi, A. Sheikhbabaei, and A.J. Seifi. 2020. Assessing the impact of climate change over the northwest of Iran: An overview of statistical downscaling methods. *Theoretical and Applied Climatology* 141: 1135–1150. https://doi.org/10.1007/s00704-020-03271-8.

Bennett, N.J. 2019. Marine social science for the peopled seas. *Coastal Management* 47 (2): 244–252. https://doi.org/10.1080/08920753.2019.1564958.

Bishop, J.M., W. Chen, A.H. Alsaffar, and H.M. Al-Foudari. 2011. Indirect effects of salinity and temperature on Kuwait's shrimp stocks. *Estuaries and Coasts* 34 (6): 1246–1254. https://doi.org/10.1007/s12237-011-9384-8.

Bouwmeester, J., R. Riera, P. Range, R. Ben-Hamadou, K. Samimi-Namin, and J.A. Burt. 2020. Coral and reef fish communities in the thermally extreme Persian/Arabian Gulf: Insights into potential climate change effects. In *Perspectives on the Marine Animal Forests of the World* (pp. 63–86). Springer, Cham. https://doi.org/10.1007/978-3-030-57054-5_3.

Brandl, S.J., J.L. Johansen, J.M. Casey, L. Tornabene, R.A. Morais, and J.A. Burt. 2020. Extreme environmental conditions reduce coral reef fish biodiversity and productivity. *Nature Communications* 11 (1): 1–14. https://doi.org/10.1038/s41467-020-17731-2.

Buchanan, J.R., F. Krupp, J.A. Burt, D.A. Feary, G.M. Ralph, and K.E. Carpenter. 2016. Living on the edge: Vulnerability of coral-dependent fishes in the Gulf. *Marine Pollution Bulletin* 105 (2): 480–488. https://doi.org/10.1016/j.marpolbul.2015.11.033.

Buchanan, J.R., G.M. Ralph, F. Krupp, H. Harwell, M. Abdallah, E. Abdulqader, M. Al-Husaini, J.M. Bishop, J.A. Burt, J.H. Choat, and B.B. Collette. 2019. Regional extinction risks for marine bony fishes occurring in the Persian/Arabian Gulf. *Biological Conservation* 230: 10–19. https://doi.org/10.1016/j.biocon.2018.11.027.

Burt, J.A. 2014. The environmental costs of coastal urbanization in the Arabian Gulf. *City* 18 (6): 760–770. https://doi.org/10.1080/13604813.2014.962889.

Burt, J.A., F. Paparella, N. Al-Mansoori, A. Al-Mansoori, and H. Al-Jailani. 2019. Causes and consequences of the 2017 coral bleaching event in the southern Persian/Arabian Gulf. *Coral Reefs* 38 (4): 567–589. https://doi.org/10.1007/s00338-019-01767-y.

Campbell, J.E., E.A. Lacey, R.A. Decker, S. Crooks, and J.W. Fourqurean. 2015. Carbon storage in seagrass beds of Abu Dhabi United Arab Emirates. *Estuaries and Coasts* 38 (1): 242–251. https://doi.org/10.1007/s12237-014-9802-9.

Campos, E.J., A.L. Gordon, B. Kjerfve, F. Vieira, and G. Cavalcante. 2020. Freshwater budget in the Persian (Arabian) Gulf and exchanges at the Strait of Hormuz. *PLoS One* 15 (5): e0233090. https://doi.org/10.1371/journal.pone.0233090.

Cavalcante, G.H., D.A. Feary, and J.A. Burt. 2016. The influence of extreme winds on coastal oceanography and its implications for coral population connectivity in the southern Arabian Gulf. *Marine Pollution Bulletin* 105 (2): 489–497. https://doi.org/10.1016/j.marpolbul.2015.10.031.

Chitsaz, N., A. Azarnivand, and S. Araghinejad. 2016. Pre-processing of data-driven river flow forecasting models by singular value decomposition (SVD) technique. *Hydrological Sciences Journal* 61 (12): 2164–2178. https://doi.org/10.1080/02626667.2015.1085991.

Chow, A.C., W. Verbruggen, R. Morelissen, Y. Al-Osairi, P. Ponnumani, H.M. Lababidi, B. Al-Anzi, and E.E. Adams. 2019. Numerical prediction of background buildup of salinity due to desalination brine discharges into the Northern Arabian Gulf. *Water* 11 (11): 2284. https://doi.org/10.3390/w11112284.

Clarke, L., K. Jiang, K. Akimoto, M. Babiker, G. Blanford, K. Fisher-Vanden, and D.P. Van Vuuren. 2014. Chapter 6 - Assessing transformation pathways. *In Climate Change 2014: Mitigation of Climate Change. IPCC Working Group III Contribution to AR5*. Cambridge University Press.

D'Agostino, D., J.A. Burt, V. Santinelli, G.O. Vaughan, A.M. Fowler, T. Reader, B.M. Taylor, A.S. Hoey, G.H. Cavalcante, A.G. Bauman, and D.A. Feary. 2021. Growth impacts in a changing ocean: Insights from two coral reef fishes in an extreme environment. *Coral Reefs* 40 (2): 433–446. https://doi.org/10.1007/s00338-021-02061-6.

Deng, T., K.W. Chau, and H.F. Duan. 2021. Machine learning based marine water quality prediction for coastal hydro-environment management. *Journal of Environmental Management* 284: 112051. https://doi.org/10.1016/j.jenvman.2021.112051.

Durack, P.J., and S.E. Wijffels. 2010. Fifty-year trends in global ocean salinities and their relationship to broad-scale warming. *Journal of Climate* 23 (16): 4342–4362. https://doi.org/10.1175/2010JCLI3377.1.

Elhakeem, A., and W. Elshorbagy. 2015. Hydrodynamic evaluation of long term impacts of climate change and coastal effluents in the Arabian Gulf. *Marine Pollution Bulletin* 101 (2): 667–685. https://doi.org/10.1016/j.marpolbul.2015.10.032.

Elhakeem, A., W.E. Elshorbagy, H. AlNaser, and F. Dominguez. 2015. Downscaling global circulation model projections of climate change for the United Arab Emirates. *Journal of Water Resources Planning and Management* 141 (9): 04015007. https://doi.org/10.1061/(ASCE)WR.1943-5452.0000507.

Elobaid, E.A., E.M. Al-Ansari, O. Yigiterhan, V.M. Aboobacker, and P. Vethamony. 2022. Spatial variability of summer hydrography in the central Arabian Gulf. *Oceanologia* 64 (1): 75–87. https://doi.org/10.1016/j.oceano.2021.09.003.

Emery, K.O. 1956. Sediments and water of Persian Gulf. *AAPG Bulletin* 40 (10): 2354–2383. https://doi.org/10.1306/5CEAE595-16BB-11D7-8645000102C1865D.

Erftemeijer, P.L., and D.A. Shuail. 2012. Seagrass habitats in the Arabian Gulf: Distribution, tolerance thresholds and threats. *Aquatic Ecosystem Health & Management* 15 (sup1): 73–83. https://doi.org/10.1080/14634988.2012.668479.

Gattuso, J.P., A. Magnan, R. Billé, W.W. Cheung, E.L. Howes, F. Joos, D. Allemand, L. Bopp, S.R. Cooley, C.M. Eakin, and O. Hoegh-Guldberg. 2015. Contrasting futures for ocean and society from different anthropogenic CO2 emissions scenarios. *Science* 349 (6243): aac4722. https://doi.org/10.1126/science.aac4722.

Gaur, S., A. Bandyopadhyay, and R. Singh. 2021. Modelling potential impact of climate change and uncertainty on streamflow projections: A case study. *Journal of Water and Climate Change* 12 (2): 384–400. https://doi.org/10.2166/wcc.2020.254.

Gebrechorkos, S.H., S. Hülsmann, and C. Bernhofer. 2019. Regional climate projections for impact assessment studies in East Africa. *Environmental Research Letters* 14 (4): 044031. https://doi.org/10.1088/1748-9326/ab055a.

Guerrero-Meseguer, L., T.E. Cox, C. Sanz-Lázaro, S. Schmid, L.A. Enzor, K. Major, F. Gazeau, and J. Cebrian. 2020. Does ocean acidification benefit seagrasses in a mesohaline environment? A mesocosm experiment in the northern gulf of Mexico. *Estuaries and Coasts* 43 (6): 1377–1393. https://doi.org/10.1007/s12237-020-00720-5.

Gupta, H.V., H. Kling, K.K. Yilmaz, and G.F. Martinez. 2009. Decomposition of the mean squared error and NSE performance criteria: Implications for improving hydrological

modelling. *Journal of Hydrology* 377 (1–2): 80–91. https://doi.org/10.1016/j.jhydrol.2009.08.003.

Haghighi, A.T., M. Sadegh, J. Bhattacharjee, M.E. Sönmez, M. Noury, N. Yilmaz, R. Noori, and B. Kløve. 2020. The impact of river regulation in the Tigris and Euphrates on the Arvandroud Estuary. *Progress in Physical Geography: Earth and Environment* 44 (6): 948–970. https://doi.org/10.1177/0309133320938676.

Hessami, M., P. Gachon, T.B. Ouarda, and A. St-Hilaire. 2008. Automated regression-based statistical downscaling tool. *Environmental Modelling & Software* 23 (6): 813–834. https://doi.org/10.1016/j.envsoft.2007.10.004.

Hong, B., and J. Shen. 2012. Responses of estuarine salinity and transport processes to potential future sea-level rise in the Chesapeake Bay. *Estuarine, Coastal and Shelf Science* 104: 33–45. https://doi.org/10.1016/j.ecss.2012.03.014.

Hume, B.C., C. D'Angelo, E.G. Smith, J.R. Stevens, J. Burt and J. Wiedenmann. 2015. Symbiodinium thermophilum sp. nov., a thermotolerant symbiotic alga prevalent in corals of the world's hottest sea, the Persian/Arabian Gulf. *Scientific Reports* 5 (1): 1–8. https://doi.org/10.1038/srep08562.

Ibrahim, H.D., P. Xue, and E.A. Eltahir. 2020. Multiple salinity equilibria and resilience of Persian/Arabian Gulf Basin salinity to brine discharge. *Frontiers in Marine Science* 7: 573. https://doi.org/10.3389/fmars.2020.00573.

Johns, W.E., F. Yao, D.B. Olson, S.A. Josey, J.P. Grist, and D.A. Smeed. 2003. Observations of seasonal exchange through the Straits of Hormuz and the inferred heat and freshwater budgets of the Persian Gulf. *Journal of Geophysical Research: Oceans* 108 (C12). https://doi.org/10.1029/2003JC001881.

Kämpf, J., and M. Sadrinasab. 2006. The circulation of the Persian Gulf: A numerical study. *Ocean Science* 2 (1): 27–41. https://doi.org/10.5194/os-2-27-2006.

Khan, N., S. Shahid, K. Ahmed, X. Wang, R. Ali, T. Ismail, and N. Nawaz. 2020. Selection of GCMs for the projection of spatial distribution of heat waves in Pakistan. *Atmospheric Research* 233: 104688. https://doi.org/10.1016/j.atmosres.2019.104688.

Kling, H., M. Fuchs, and M. Paulin. 2012. Runoff conditions in the upper Danube basin under an ensemble of climate change scenarios. *Journal of Hydrology* 424: 264–277. https://doi.org/10.1016/j.jhydrol.2012.01.011.

Knoben, W.J., J.E. Freer, and R.A. Woods. 2019. Inherent benchmark or not? Comparing Nash-Sutcliffe and Kling-Gupta efficiency scores. *Hydrology and Earth System Sciences* 23 (10): 4323–4331. https://doi.org/10.5194/hess-23-4323-2019.

Lachkar, Z., M. Lévy, and K.S. Smith. 2019. Strong intensification of the Arabian Sea oxygen minimum zone in response to Arabian Gulf warming. *Geophysical Research Letters* 46 (10): 5420–5429. https://doi.org/10.1029/2018GL081631.

Lee, W., and J.M. Kaihatu. 2018. Effects of Desalination on hydrodynamic process in Persian Gulf. *Coastal Engineering Proceedings* 36: 3–3. https://doi.org/10.9753/icce.v36.papers.3.

L'Hégaret, P., R. Duarte, X. Carton, C. Vic, D. Ciani, R. Baraille, and S. Corréard. 2015. Mesoscale variability in the Arabian Sea from HYCOM model results and observations: Impact on the Persian Gulf water path. *Ocean Science* 11 (5): 667–693. https://doi.org/10.5194/os-11-667-2015.

Lioubimtseva, E., and R. Cole. 2006. Uncertainties of climate change in arid environments of Central Asia. *Reviews in Fisheries Science* 14 (1–2): 29–49. https://doi.org/10.1080/10641260500340603.

Liu, D.L., and O'leary, G. J., Christy, B., Macadam, I., Wang, B., Anwar, M. R., and Weeks, A. 2017. Effects of different climate downscaling methods on the assessment of climate change impacts on wheat cropping systems. *Climatic Change* 144 (4): 687–701. https://doi.org/10.1007/s10584-017-2054-5.

Liu, Z., Z. Xu, S.P. Charles, G. Fu, and L. Liu. 2011. Evaluation of two statistical downscaling models for daily precipitation over an arid basin in China. *International Journal of Climatology* 31 (13): 2006–2020. https://doi.org/10.1002/joc.2211.

Lorenz, M., K. Klingbeil, and H. Burchard. 2020. Numerical study of the exchange flow of the Persian Gulf using an extended total exchange flow analysis framework. *Journal of Geophysical Research: Oceans* 125 (2): e2019JC015527. https://doi.org/10.1029/2019JC015527.

Luyten, P.J., J.E. Jones, R. Proctor, A. Tabor, P. Tett and K. Wild-Allen. 1999. COHERENS–A coupled hydrodynamical-ecological model for regional and shelf seas: User documentation. *MUMM Report, Management Unit of the Mathematical Models of the North Sea* 914.

Moradi, M. 2020. Trend analysis and variations of sea surface temperature and chlorophyll-a in the Persian Gulf. *Marine Pollution Bulletin* 156: 111267. https://doi.org/10.1016/j.marpolbul.2020.111267.

Moriasi, D.N., J.G. Arnold, M.W. Van Liew, R.L. Bingner, R.D. Harmel, and T.L. Veith. 2007. Model evaluation guidelines for systematic quantification of accuracy in watershed simulations. *Transactions of the ASABE* 50 (3): 885–900. https://doi.org/10.13031/2013.23153.

Nash, J.E., and J.V. Sutcliffe. 1970. River flow forecasting through conceptual models part I—A discussion of principles. *Journal of Hydrology* 10 (3): 282–290. https://doi.org/10.1016/0022-1694(70)90255-6.

NOAA National centers for environmental information, state of the climate: Global climate report for annual. 2019, published online January 2020. Retrieved on December 30, 2020 from https://www.ncdc.noaa.gov/sotc/global/201913.

Noori, R., F. Tian, R. Berndtsson, M.R. Abbasi, M.V. Naseh, A. Modabberi, A. Soltani, and B. Kløve. 2019. Recent and future trends in sea surface temperature across the Persian Gulf and Gulf of Oman. *PLoS One* 14 (2): e0212790. https://doi.org/10.1371/journal.pone.0212790.

Pahlavan, H.A., B. Zahraie, M. Nasseri, and A.M. Varnousfaderani. 2018. Improvement of multiple linear regression method for statistical downscaling of monthly precipitation. *International Journal of Environmental Science and Technology* 15 (9): 1897–1912. https://doi.org/10.1007/s13762-017-1511-z.

Pal, J.S., and E.A. Eltahir. 2016. Future temperature in southwest Asia projected to exceed a threshold for human adaptability. *Nature Climate Change* 6 (2): 197. https://doi.org/10.1038/nclimate2833.

Paparella, F., C. Xu, G.O. Vaughan, and J.A. Burt. 2019. Coral bleaching in the Persian/Arabian Gulf is modulated by summer winds. *Frontiers in Marine Science* 6: 205. https://doi.org/10.3389/fmars.2019.00205.

Phillips, H.E., A. Tandon, R. Furue, R. Hood, C.C. Ummenhofer, J.A. Benthuysen, V. Menezes, S. Hu, B. Webber, A. Sanchez-Franks, and D. Cherian. 2021. Progress in understanding of Indian Ocean circulation, variability, air–sea exchange, and impacts on biogeochemistry. *Ocean Science* 17 (6): 1677–1751. https://doi.org/10.5194/os-17-1677-2021.

Pous, S., P. Lazure, and X. Carton. 2015. A model of the general circulation in the Persian Gulf and in the Strait of Hormuz: Intraseasonal to interannual variability. *Continental Shelf Research* 94: 55–70. https://doi.org/10.1016/j.csr.2014.12.008.

Ranjbar, M.H., A. Etemad-Shahidi, and B. Kamranzad. 2020. Modeling the combined impact of climate change and sea-level rise on general circulation and residence time in a semi-enclosed sea. *Science of the Total Environment* 140073. https://doi.org/10.1016/j.scitotenv.2020.140073.

Rashid, M.M., S. Beecham, and R.K. Chowdhury. 2015. Statistical downscaling of CMIP5 outputs for projecting future changes in rainfall in the Onkaparinga catchment. *Science of the Total Environment* 530: 171–182. https://doi.org/10.1016/j.scitotenv.2015.05.024.

Riegl, B., M. Johnston, S. Purkis, E. Howells, J. Burt, S.C. Steiner, C.R. Sheppard, and A. Bauman. 2018. Population collapse dynamics in Acropora downingi, an Arabian/Persian Gulf ecosystem-engineering coral, linked to rising temperature. *Global Change Biology* 24 (6): 2447–2462. https://doi.org/10.1111/gcb.14114.

Riegl, B., and S. Purkis. 2015. Coral population dynamics across consecutive mass mortality events. *Global Change Biology* 21 (11): 3995–4005. https://doi.org/10.1111/gcb.13014.

Rixen, T., G. Cowie, B. Gaye, J. Goes, and H. Do Rosário Gomes, R.R. Hood, Z. Lachkar, H. Schmidt, J. Segschneider, and A. Singh. 2020. Reviews and syntheses: Present, past, and future of the oxygen minimum zone in the northern Indian Ocean. *Biogeosciences* 17 (23): 6051–6080. https://doi.org/10.5194/bg-17-6051-2020.

Reynolds, R.M. 1993. Physical oceanography of the Gulf, Strait of Hormuz, and the Gulf of Oman—Results from the Mt Mitchell expedition. *Marine Pollution Bulletin* 27: 35–59. https://doi.org/10.1016/0025-326X(93)90007-7.

Sada, R., B. Schmalz, J. Kiesel, and N. Fohrer. 2019. Projected changes in climate and hydrological regimes of the Western Siberian lowlands. *Environmental Earth Sciences* 78 (2): 56. https://doi.org/10.1007/s12665-019-8047-0.

Sala, O.E., F.I.I.I. Stuart Chapin, J.J. Armesto, E. Berlow, J. Bloomfield, R. Dirzo, E. Huber-Sanwald, L.F. Huenneke, R.B. Jackson, A. Kinzig and R. Leemans. 2000. Global biodiversity scenarios for the year 2100. S*cience* 287 (5459): 1770–1774. https://doi.org/10.1126/science.287.5459.1770.

Salimi, M., and S.G. Al-Ghamdi. 2020. Climate change impacts on critical urban infrastructure and urban resiliency strategies for the Middle East. *Sustainable Cities and Society* 54: 101948. https://doi.org/10.1016/j.scs.2019.101948.

Schott, F.A., and J.P. McCreary Jr. 2001. The monsoon circulation of the Indian Ocean. *Progress in Oceanography* 51 (1): 1–123. https://doi.org/10.1016/S0079-6611(01)00083-0.

Sedigh Marvasti, S., A. Gnanadesikan, A.A. Bidokhti, J.P. Dunne, and S. Ghader. 2016. Challenges in modeling spatiotemporally varying phytoplankton blooms in the Northwestern Arabian Sea and Gulf of Oman. *Biogeosciences* 13 (4): 1049–1069. https://doi.org/10.5194/bg-13-1049-2016.

Shamshirband, S., E. Jafari Nodoushan, J.E. Adolf, A. Abdul Manaf, A. Mosavi, and K.W. Chau. 2019. Ensemble models with uncertainty analysis for multi-day ahead forecasting of chlorophyll a concentration in coastal waters. *Engineering Applications of Computational Fluid Mechanics* 13 (1): 91–101. https://doi.org/10.1080/19942060.2018.1553742.

Sheehan, P.M., B.G. Webber, A. Sanchez-Franks, A.J. Matthews, K.J. Heywood, and P.N. Vinayachandran. 2020. Injection of oxygenated Persian Gulf Water into the southern Bay of Bengal. *Geophysical Research Letters* 47 (14): e2020GL087773. https://doi.org/10.1029/2020GL087773.

Swift, S.A., and A.S. Bower. 2003. Formation and circulation of dense water in the Persian/Arabian Gulf. *Journal of Geophysical Research: Oceans* 108 (C1): 4–1. https://doi.org/10.1029/2002JC001360.

Taylor, K.E. 2001. Summarizing multiple aspects of model performance in a single diagram. *Journal of Geophysical Research: Atmospheres* 106 (D7): 7183–7192. https://doi.org/10.1029/2000JD900719.

Taylor, K.E., R.J. Stouffer, and G.A. Meehl. 2012. An overview of CMIP5 and the experiment design. *Bulletin of the American Meteorological Society* 93 (4): 485–498. https://doi.org/10.1175/BAMS-D-11-00094.1.

Tegegne, G., A.M. Melesse, and A.W. Worqlul. 2020. Development of multi-model ensemble approach for enhanced assessment of impacts of climate change on climate extremes. *Science of the Total*

Environment 704: 135357. https://doi.org/10.1016/j.scitotenv.2019.135357.

Thoppil, P.G., and P.J. Hogan. 2010. A modeling study of circulation and eddies in the Persian Gulf. *Journal of Physical Oceanography* 40 (9): 2122–2134. https://doi.org/10.1175/2010JPO4227.1.

Trott, C.B., B. Subrahmanyam, V.S.N. Murty, and J.F. Shriver. 2019. Large-scale fresh and salt water exchanges in the Indian Ocean. *Journal of Geophysical Research: Oceans* 124 (8): 6252–6269. https://doi.org/10.1029/2019JC015361.

Vasou, P., V. Vervatis, G. Krokos, I. Hoteit, and S. Sofianos. 2020. Variability of water exchanges through the Strait of Hormuz. *Ocean Dynamics* 70 (8): 1053–1065. https://doi.org/10.1007/s10236-020-01384-2.

Vaughan, G.O., N. Al-Mansoori, and J.A. Burt. 2019 The Arabian Gulf. In: Sheppard, C., Ed., *World Seas: An Environmental Evaluation*, Vol. 2: *The Indian Ocean to the Pacific*. Chapter 1, 1–23, 2nd edn. Cambridge: Academic Press. https://doi.org/10.1016/B978-0-08-100853-9.00001-4.

Wabnitz, C.C., V.W. Lam, G. Reygondeau, L.C. Teh, D. Al-Abdulrazzak, M. Khalfallah, D. Pauly, M.L.D. Palomares, D. Zeller, and W.W. Cheung. 2018. Climate change impacts on marine biodiversity, fisheries and society in the Arabian Gulf. *PLoS ONE* 13 (5): e0194537. https://doi.org/10.1371/journal.pone.0194537.

Waltham, N.J., M. Elliott, S.Y. Lee, C. Lovelock, C.M. Duarte, C. Buelow, C. Simenstad, I. Nagelkerken, L. Claassens, C.K. Wen, and M. Barletta. 2020. UN decade on ecosystem restoration 2021–2030—What chance for success in restoring coastal ecosystems?. *Frontiers in Marine Science* p.71. https://doi.org/10.3389/fmars.2020.00071.

Wang, R., Q. Cheng, L. Liu, C. Yan, and G. Huang. 2019. Multi-model projections of climate change in different RCP scenarios in an arid inland region Northwest China. *Water* 11 (2): 347. https://doi.org/10.3390/w11020347.

Wang, S., H. Yang, Q.B. Pham, D.N. Khoi, and P.T.T. Nhi. 2020. An ensemble framework to investigate wind energy sustainability considering climate change impacts. *Sustainability* 12 (3): 876. https://doi.org/10.3390/su12030876.

Wilby, R.L., and C.W. Dawson. 2013. The statistical downscaling model: Insights from one decade of application. *International Journal of Climatology* 33 (7): 1707–1719. https://doi.org/10.1002/joc.3544.

Wilby, R.L., C.W. Dawson, and E.M. Barrow. 2002. SDSM—A decision support tool for the assessment of regional climate change impacts. *Environmental Modelling & Software* 17 (2): 145–157. https://doi.org/10.1016/S1364-8152(01)00060-3.

Wilby, R.L., L.E. Hay, and G.H. Leavesley. 1999. A comparison of downscaled and raw GCM output: Implications for climate change scenarios in the San Juan River basin Colorado. *Journal of Hydrology* 225 (1–2): 67–91. https://doi.org/10.1016/S0022-1694(99)00136-5.

Xue, P., and E.A. Eltahir. 2015. Estimation of the heat and water budgets of the Persian (Arabian) Gulf using a regional climate model. *Journal of Climate* 28 (13): 5041–5062. https://doi.org/10.1175/JCLI-D-14-00189.1.

Yao, F., and W.E. Johns. 2010. A HYCOM modeling study of the Persian Gulf: 1. Model configurations and surface circulation. *Journal of Geophysical Research: Oceans* 115 (C11). https://doi.org/10.1029/2009JC005781.

Zamani, R., and R. Berndtsson. 2019. Evaluation of CMIP5 models for west and southwest Iran using TOPSIS-based method. *Theoretical and Applied Climatology* 137 (1): 533–543. https://doi.org/10.1007/s00704-018-2616-0.

Zimmerman, R.C. 2021. Scaling up: Predicting the impacts of climate change on seagrass ecosystems. *Estuaries and Coasts* 44 (2): 558–576. https://doi.org/10.1007/s12237-020-00837-7.